Natarajan, N.; Xu, C.; Dowd, P.A.; Hand, M.
Numerical modelling of thermal transport and quartz precipitation/dissolution in a coupled fracture-skin-matrix system
International Journal of Heat and Mass Transfer, 2014; 78:302-310

http://dx.doi.org/10.1016/j.ijheatmasstransfer.2014.06.085

Numerical modelling of thermal transport and quartz precipitation/dissolution in a coupled fracture-skin-matrix system

[1]N. Natarajan, [2]Chaoshui Xu, [3]Peter A. Dowd, [4]Martin Hand

[1] Assistant Professor, Department of Civil Engineering, MVGR College of Engineering, Chintalavalasa, Vizianagaram, Andhra Pradesh, India.

[2] Associate Professor, School of Civil, Environmental and Mining Engineering, University of Adelaide, Adelaide, South Australia, SA 5005, Australia.

[3] Professor, School of Civil, Environmental and Mining Engineering, University of Adelaide, Adelaide, South Australia, SA 5005, Australia.

[4] Director, South Australian Centre for Geothermal Energy Research, University of Adelaide, Adelaide, South Australia, SA 5005, Australia.

Abstract

This paper describes a numerical model for the analysis of chemical reactions in a coupled fracture-matrix system at the scale of a single fracture in the presence of fracture-skin. The quartz concentration is computed using simple linear reaction kinetics. Heat transfer within the fracture-skin and rock matrix is modelled as conduction, while heat transport within the fracture includes thermal advection, conduction, and dispersion in the horizontal plane. Fluid is assumed to be injected at a constant rate at the inlet of the fracture. Heat transfer at the interface of the high permeability fracture and low permeability fracture-skin is modelled on a varying grid at the interface. Sensitivity studies have been conducted using different skin thermal conductivities, fluid velocities, and half fracture apertures. We have also analysed the behaviour of the system when there is fluid loss from the fracture into the adjacent fracture skin. Results suggest that, when fluid loss is considered, the rate at which fluid is injected at the inlet of the fracture plays a major role in the heat transfer and chemical reaction within the fracture. When there is fluid loss, the effect of fracture skin formation on the heat transfer mechanism is reduced and this effect

becomes much less sensitive to changes in the size of the fracture aperture. The fracture skin thickness affects the attainment of equilibrium temperature within the fracture in terms of its magnitude and distance from the fracture inlet.

Keywords: Fracture-skin; Fracture aperture; Reactive mineral transport; Thermal transport.

Introduction

Hot Dry Rock (HDR) is a potential source of substantial amounts of renewable energy due to its wide-spread distribution and the extent of individual occurrences. The energy is extracted by creating a connected fracture network in the HDR heat reservoir through which fluid is circulated to extract the heat. An effective fracture network allowing sufficient fluid flow (and, thereby, sufficient heat extraction) creates an engineered (or enhanced) geothermal system (EGS). When fluid moves through a fracture it reacts with the adjacent rock-matrix resulting in precipitation-dissolution of minerals due to the high temperature gradient between the high permeability fracture and low permeability rock-matrix. Over the past 30 years there have been many publications on this precipitation-dissolution process [1-12] and many studies have been reported on fracture-matrix coupled systems.

Most studies on thermal transport in fractured formations do not consider the presence of fracture skins. Moench [13, 14] defined fracture skins to be low permeability material deposited on the fracture walls which mitigates the diffusive mass transfer between the high and low permeability materials. Sharp [15] noted the formation of skins in fractured porous media. Later studies concluded that fracture skins can occur as clay filling [16], mineral precipitation [17] and organic material growth [18]. Thus, the formation of fracture-skin can affect the heat transport

mechanism in fractured porous media as the properties of the fracture-skin, such as porosity and diffusion, can differ significantly from that of the surrounding rock-matrix. The differences in the properties of the fracture-skin from those of the associated rock-matrix result in different diffusive mechanisms at the fracture-skin interface from those at the skin-matrix interface. The formation of skin during thermal transport in a fracture matrix system is caused by the deposition on the fracture walls of chemicals undergoing precipitation due to high temperatures. The interchange of solutes between the fracture and the matrix causes precipitation of metal oxides [17] or calcite [19, 20]. Natarajan and Kumar [21] illustrated this by using a numerical model to analyse the effect of fracture-skin formation on thermal transport in fractured porous media and concluded that the fracture-skin plays a major role in the heat transfer between the fracture and the associated rock-matrix. Natarajan and Kumar [22] studied the evolution of fracture permeability in a coupled fracture-matrix system in the presence of fracture-skin due to co-colloidal bacterial transport in a geothermal system. However, they did not consider the effect of fluid loss from the fracture into the adjacent fracture skin. The objective of the work presented here is to include the effect of fluid loss from the fracture in the analysis of the mineral precipitation process in fractured porous media in the presence of fracture skin for various fracture apertures, fluid velocities and skin thermal conductivities.

Physical system and governing equations

A conceptual model of a coupled fracture-skin-matrix system [23] is given in Fig.1.

Figure 1 to be inserted here

In Figure 1, b is the half fracture aperture, d-b is the thickness of the fracture-skin and H is the thickness of the half fracture spacing. The following assumptions are made:

1. The fracture aperture is much smaller than the length of the fracture.
2. Thermal dispersion is analogous to dispersion of solutes in a fracture matrix system.
3. Convection within the fracture-skin and rock-matrix can be ignored.
4. Temperature at the fracture-skin interface, i.e., temperatures along the fracture wall and along the lower boundary of the fracture-skin are assumed to be equal (at y = b).
5. Temperature at the skin-matrix interface, i.e., temperatures along the upper boundary of the fracture-skin and the lower boundary of the rock-matrix are assumed to be equal (at y = d). The conductive flux in the fracture-skin is equal to the conductive flux in the rock-matrix at the skin-matrix interface as expressed in equation (10).
6. Specific heat capacities are not functions of temperature.
7. Assuming symmetry, the solution is restricted to one half of the fracture and its adjacent fracture-skin and its associated rock-matrix.
8. Thermal conduction is considered both in the fracture, fracture skin and the rock-matrix.
9. There is only one fluid phase.
10. Changes in fluid enthalpy with pressure are neglected.
11. Transverse diffusion and dispersion within the fracture ensure complete mixing across the fracture thickness/aperture at all times.
12. Transport along the fracture is much faster than transport within the rock matrix and fracture skin.

Fluid flow

The momentum balance states that the flow average velocity is proportional to the pressure gradient:

$$q = \frac{b^3}{12\mu}\frac{\partial p}{\partial x} \quad (1)$$

where μ is the viscosity, b is the half fracture aperture, p is the pressure within the fracture caused by the injection, q is the volumetric flow rate per unit width of the fracture given by:

$$q = b*v \quad (2)$$

where v is the velocity of the fluid.

The continuity of the fluid considering fluid loss from the fracture wall into the fracture skin is:

$$\frac{\partial q}{\partial x} + 2q_l = 0 \quad (3)$$

where q_l is the fluid loss velocity which has been kept as constant along the fracture [24]. Rawal and Ghassemi [24] assumed that fluid loss at the interface is instantaneous and the same assumption has been used in this study.

Heat transport

The principal transport mechanisms in the fracture include thermal convection, conduction and dispersion, in addition to heat transfer from the fracture into the fracture-skin. As the migration of fluid is faster along the high permeability fracture, transport of heat is assumed to be one-dimensional along the fracture. The coupling between the fracture and skin is ensured by the continuity of the fluxes between them by assuming that the conductive flux from the fracture to the fracture-skin takes place in a direction perpendicular to the fracture. Conductive exchanges in the direction parallel to the fracture plane are assumed to be negligible compared with that

perpendicular to the fracture plane. For relatively low injection rates it is reasonable to assume that heat conduction in the fracture-skin is one-dimensional perpendicular to the fracture [25].

The thermal transport equations for the coupled fracture matrix system provided by de Marsily(1986) has been modified for the fracture-skin-matrix system.

$$\frac{\partial T_f}{\partial t} = -v\frac{\partial T_f}{\partial x} + D_f\frac{\partial^2 T_f}{\partial x^2} + D_T\frac{\partial^2 T_f}{\partial x^2} + \frac{\lambda_s}{\rho_f c_f b}\frac{\partial T_s}{\partial y}\bigg|_{y=b} \tag{4}$$

$$\frac{\partial T_s}{\partial t} = \frac{\lambda_s}{\rho_s c_s}\frac{\partial^2 T_s}{\partial y^2} \tag{5}$$

$$\frac{\partial T_m}{\partial t} = \frac{\lambda_m}{\rho_m c_m}\frac{\partial^2 T_m}{\partial y^2} \tag{6}$$

$$D_T = v * \beta_T \tag{7}$$

$$D_f = \frac{\lambda_f}{\rho_f c_f} \tag{8}$$

where T_f, T_s, T_m are the relative temperatures in the fracture, skin and the rock-matrix respectively. D_T is the thermal dispersion coefficient in the fracture [26]. D_f is the thermal conduction coefficient of the fluid in the fracture, v is the velocity of the fluid in the fracture; β_T is the thermal dispersivity; λ_f is the thermal conductivity of the fluid in the fracture, λ_s is the thermal conductivity of the fracture-skin and λ_m is the thermal conductivity of the reservoir matrix; ρ_f, ρ_s and ρ_m are the densities of the fracture, fracture-skin and rock-matrix; c_f, c_s and c_m are the specific heat capacities of the fracture, fracture-skin and rock-matrix; b is the half fracture aperture.

Equation (4) represents the thermal transport in the fracture. Equations (5) and (6) represent the transport processes in the immobile zones of the fracture-skin and rock-matrix respectively. Thermal convection in the fracture is represented by the first term in equation (4), thermal conduction and dispersion by second and third terms. The last term represents the coupling between the fracture and the fracture-skin. The initial and boundary conditions associated with equations (4), (5) and (6) are:

$$T_f(x,t=0) = T_s(x,y,t=0) = T_m(x,y,t=0) = 1.0 \tag{9}$$

$$T_f(x=0,t) = 0.5 \tag{10}$$

$$T_f(x=L_f,t) = 1.0 \tag{11}$$

$$T_f(x,t) = T_s(x,y=b,t) \tag{12}$$

$$\lambda_s \frac{\partial T_s(x,y=d,t)}{\partial y} = \lambda_m \frac{\partial T_m(x,y=d,t)}{\partial y} \tag{13}$$

$$T_s(x,y=d,t) = T_m(x,y=d,t) \tag{14}$$

$$\frac{\partial T_m(x,y=H,t)}{\partial y} = 0 \tag{15}$$

Precipitation – Dissolution

The temperature dependent equilibrium concentration of quartz adopted by Pendergrass and Robinson [2] from Rimstidt and Barnes [27] is

$$C^{eq} = 6*10^4 * 10^{\left(1.881 - 2.028*10^{-3}T - 1560/T\right)} \tag{16}$$

where equilibrium concentration is in ppm and temperature is in K.

The temperature dependent dissolution rate constant is given by Robinson [1]

$$k = 10^{\left(0.433 - 4090/T\right)} \tag{17}$$

where the units of k are $m.s^{-1}$.

The initial condition for pressure in the fracture is given by:

$$p\,(x,t=0) = 0 \qquad (18)$$

The rate at which water is injected at the injection well is assumed to be 1e-03 $m^3.d^{-1}$ (q_0) and the fluid loss rate is assumed to be 1e-05 $m.d^{-1}$.

Numerical model

In this study, the system is described by a set of three partial differential equations, one equation for the fracture, one for the fracture-skin and one for the rock-matrix. The coupled non-linear equations are solved numerically using an implicit finite difference scheme. Continuity at the fracture-skin interface is achieved by iterating the solution at each time step. A uniform grid is used for the fracture and a non-uniform grid is used for the fracture-skin. A smaller grid size is used in the fracture-skin interface to capture accurately the heat flux transfer at the fracture-skin interface. The dissolution rate constants for fracture (K_f), fracture-skin (K_s) and rock-matrix (K_m) are determined from the temperature distribution obtained for the fracture, fracture-skin and the rock-matrix using Eqn. (17).

The initial temperature of the fracture, fracture-skin and rock-matrix is assumed to be 600K which is expressed in terms of relative temperature. At the entry to the fracture the fluid has a relative temperature of 0.5, corresponding to a temperature of 300K.

The discharge along the fracture is calculated from the assumed discharge rate at the entry to the fracture (inlet) and the fluid loss rate. This information is used to obtain the velocity distribution is along the fracture using Eqn. (2) which includes fluid loss term. For the non fluid loss case, the velocity along the fracture is kept constant as the discharge remains constant. The velocity

distribution obtained is used in Eqn. (4) to determine the temperature distribution along the fracture.

Results and discussions

The mineral precipitation in the coupled fracture matrix system with fracture skin is analysed in the presence and absence of fracture fluid loss. The parameters used for numerical simulation are given in Table 1.

Table 1 to be inserted here

Figure 2 to be inserted here

The results for the verification of the numerical model for thermal transport are shown in Fig. 2. The results obtained by Kumar and Ghassemi [9] are shown by symbols, while the numerical results obtained using the present model are plotted as solid lines. Figure 2 shows that the results from the present model are in close agreement from those obtained by Kumar and Ghassemi [9].

Figure 3 to be inserted here

Figure 3 provides a comparison of the spatial distribution of quartz concentration obtained along the fracture in the presence and absence of fracture skin, without fluid loss. When fracture skin is present, quartz attains equilibrium concentration much closer to the fracture inlet than it does when there is no fracture skin. The fracture skin significantly affects the heat transfer mechanism and consequently quartz dissolution is much quicker in the presence of fracture skin. Thus, it is always important to include the fracture skin while analysing non-isothermal processes in a coupled fracture matrix system.

Temperature distribution

The temperature distribution along the fracture was analysed for various media and flow parameters such as skin thermal conductivity, fluid velocity, fracture aperture and inlet discharges.

Figure 4 (a) and (b) to be inserted here

Figures 4(a) and 4(b) show the spatial distributions of relative temperature along the fracture for various skin thermal conductivities in the absence and presence of fluid loss. Figure 4(a) shows that temperature attains equilibrium within a short period of time when the skin thermal conductivity is high (i.e. λ_s = 10 W.(m-K)$^{-1}$). This is due to presence of the fracture skin, the high thermal conductivity of which enhances thermal transfer from the rock matrix to the fracture. The equilibrium state is attained at a relative temperature of 0.95 compared to other cases where the equilibrium is attained beyond 0.95. As the skin thermal conductivity is reduced, the distance from the inlet of the fracture at which equilibrium temperature is attained increases. For a skin thermal conductivity of 2 W.(m-K)$^{-1}$, the equilibrium temperature of 1 is attained at 5m (approximately) from the inlet. The temperature and the distance from the inlet at which equilibrium is attained vary with the skin thermal conductivity. Therefore, the magnitude of the skin thermal conductivity plays an important role in the heat and mass transfer in fractured porous media. The temperature profiles in Figure 4(b) with no fluid loss are very similar to those in Figure 4(a) with fluid loss but equilibrium temperature is attained farther away from the fracture inlet. This is because when there is fluid loss from the fracture, the fluid velocity varies

due to varying discharge. As a result, the time taken for the temperature to attain equilibrium is longer as can be seen in Figure 4(b). Thus fluid loss from the fracture into the fracture skin plays a significant role in heat transfer and it is recommended that fluid loss from the fracture is included in modelling the heat transfer process in geothermal systems. Furthermore, as can be seen in Figure 4 (b), the magnitude of the equilibrium temperature attained and the distance at which it is attained from the fracture inlet vary with respect to the fracture skin thickness. Therefore, the fracture skin thickness affects the attainment of equilibrium temperature within the fracture in terms of its magnitude and distance from the fracture inlet. This is an important result that has not previously been reported in the literature.

Figure 5 to be inserted here

Figure 5 shows the spatial distributions of relative temperature along the fracture for various initial fluid velocities. When the initial fluid velocity is low, equilibrium temperature is attained within a short distance of 5m from the fracture inlet. The low fluid velocity provides high residence time for the transfer of heat from the fracture-skin to the fracture and therefore equilibrium state is attained close to the inlet of the source. As the fluid velocity is increased, the distance at which equilibrium temperature is attained increases from the inlet of the fracture. When the initial fluid velocity is high (10 $m.d^{-1}$), it takes a significant amount of time for the fluid to attain equilibrium temperature as the residence time available for the fluid is low and thus heat transfer between the fracture-skin and fracture is slow. The results obtained in this case without fluid loss from the fracture has not been compared to the results with fluid loss since the fluid velocity continuously varies along the fracture due to the fluid loss and thus the comparison of the results would not be meaningful.

Figure 6 (a) and (b) to be inserted here

Figures 6 (a) and (b) show the spatial distributions of relative temperature along the fracture for various half fracture apertures (a) without fluid loss and (b) with fluid loss. In Figure 6 (a) it can be seen that when the half fracture aperture is low (b = 50μm), the fluid attains equilibrium temperature close to the fracture inlet since the coupling between the fracture and the fracture-skin is strong and therefore the heat transfer is more intense. As the half fracture aperture increases, the fluid takes a longer time to attain equilibrium temperature as the interaction between the fracture and the fracture-skin becomes progressively weaker. For a half fracture aperture of 500μm, the fluid attains equilibrium temperature at 15m from the fracture inlet. Therefore, when the fracture aperture is large, the fracture-skin-matrix system becomes decoupled and it behaves as a single fracture. Thus, fracture-skin is ineffective when the half fracture aperture is large.

Figure 6(b) shows the relative temperature along the fracture when fluid loss from the fracture is considered. It can be seen that in the presence of fluid loss, the equilibrium temperature is attained at about 20m from the fracture inlet for various half-fracture apertures but is attained at different distances from the inlet of the fracture in the absence of fluid loss. It is interesting to note that in the presence of fluid loss the relative temperature profiles for different half-fracture apertures follow a similar pattern. Therefore, when fluid loss is considered, the temperature distribution is not sensitive to the variation in the half-fracture aperture. The varying fluid velocity plays a dominant role compared to the fracture aperture due to the loss of fluid from the fracture. Moreover, in the presence of fluid loss, the equilibrium temperature attained by the

fluid for different half-fracture apertures is 0.95 unlike the case of no fluid loss for which the equilibrium temperature of 1 is attained by the fluid for different apertures. When there is continuous loss of fluid from the fracture to its surrounding fracture skin, it takes a longer time for the temperature to attain equilibrium, as can be seen by comparing Figure 6(b) with Figure 6(a). The equilibrium condition with fluid loss is attained at approximately 20m from the fracture inlet for all cases examined. Therefore, when there is fluid loss, the effect of fracture skin formation on the heat transfer mechanism is reduced. In addition, the attained equilibrium temperature and the distance of the attainment from the inlet become much less sensitive to the size of the fracture aperture, which is an important result from this study.

Figure7 to be inserted here

Figure 7 shows the spatial distributions of relative temperature along the fracture for various rates of inlet discharge for a fracture length of 100m. Figure 7 shows that when water is pumped at a very low rate, the equilibrium temperature is attained close to the fracture inlet as the fluid velocity is low and the heat transfer is quicker. As the discharge rate at the inlet is increased, the distance at which equilibrium temperature is attained in the fracture also increases from the inlet. As discharge increases, the fluid velocity also increases indicating that it would take a longer time for the fluid to access the heat from the fracture-skin. For a high inlet discharge of 0.005 $m^3.d^{-1}$, the equilibrium temperature is nearer to the fracture outlet. Therefore, the rate at which the fluid is pumped at the inlet also affects the heat transfer mechanism in the coupled fracture-skin-matrix system with fluid loss. The results obtained in the absence of fluid loss have not been compared with those obtained with fluid loss as the discharge remains constant when there is no

loss of fluid. As the discharge remains constant, the fluid velocity will also be constant. Thus, the temperature distribution profiles would remain constant along the fracture irrespective of the discharge along the fracture.

Quartz concentration

The quartz concentration along the fracture was analysed for various media and flow parameters such as skin thermal conductivity, fluid velocity, fracture aperture and inlet discharges.

Figure 8 (a) and (b) to be inserted here

Figures 8(a) and (b) show the spatial distributions of quartz concentration along the fracture for various skin thermal conductivities in the absence and presence of fluid loss. Figure 8(a) shows that quartz attains equilibrium concentration within a short period when the skin thermal conductivity is high (i.e. λ_s = 10 W.(m-K)$^{-1}$). This is because the presence of skin significantly enhances the thermal transfer from the fracture skin to the fracture thereby accelerating the rate of quartz dissolution along the fracture. Moreover, it attains equilibrium concentration at 10mM.l^{-1} compared to the other cases for which the equilibrium concentration is attained beyond 10mM.l^{-1}. When skin thermal conductivity is 4 W.(m-K)$^{-1}$ and 6 W.(m-K)$^{-1}$, the equilibrium concentration is attained at about the same distance from the inlet of the fracture as that of skin with thermal conductivity 2 W.(m-K)$^{-1}$, but the magnitude of the quartz equilibrium concentration is different since the thermal distribution profiles are different for different skin thermal conductivities. The magnitude of the skin thermal conductivity plays an important role in the mineral precipitation in fractured porous media. The presence of fracture-skin can enhance

the heat transfer mechanism and thereby increase the permeability of the fractures in a geothermal system. The concentration profiles in Figure 8(b) are very similar to those in Figure 8(a) but equilibrium concentration is attained farther away from the fracture for different skin thermal conductivities. When there is no fluid loss the equilibrium concentration is attained at about 5m from the inlet but when there is fluid loss the equilibrium concentration is attained 25m from the inlet of the fracture. This is because the time taken for the temperature to attain equilibrium is longer as can be seen in Figure 4 (b) and consequently the chemical reactions are delayed. Therefore, the fluid loss from the fracture plays a significant role in the chemical reactivity of a geothermal system.

Figure 9 to be inserted here

Figure 9 shows the spatial distributions of quartz concentration along the fracture for various initial fluid velocities. When the initial fluid velocity is low, equilibrium quartz concentration is attained within a short distance from the fracture inlet as the temperature within the fracture quickly attains equilibrium. As the fluid velocity is increased, the distance from the inlet of the fracture at which equilibrium concentration is attained increases. When the initial fluid velocity is high (10 $m.d^{-1}$), it takes a long time for the mineral to equilibrium concentration because of the slower heat transfer between the fracture-skin and the fracture as shown in Figure 5. The results obtained in this case, without fracture fluid loss, have not been compared to the results with fluid loss since the fluid velocity varies continuously along the fracture due to the fluid loss and it is not appropriate to compare these results.

Figure 10 (a) and (b) to be inserted here

Figures 10 (a) and (b) show the spatial distributions of quartz concentration along the fracture for various half fracture apertures with and without fluid loss. From Figure 10 (a), when the half fracture aperture is low (b = 50μm), equilibrium concentration is attained close to the fracture inlet as the heat transfer between the fracture and the fracture-skin is very effective as shown in figure 6. As the half fracture aperture increases, the mineral takes a longer time to equilibrium concentration as the interaction between the fracture and the fracture-skin weakens. Thus, fracture-skin can increase the chemical reactions in a geothermal system when the fracture apertures are small. This can effectively increase the permeability and consequently the efficiency of the system. Figure 10(b) shows the quartz concentration for the case of fracture fluid loss from which it can be seen that the equilibrium concentration is attained at about 20m from the fracture inlet for various half fracture apertures but in the absence of fluid loss equilibrium is attained at different distances from the inlet of the fracture. In the presence of fluid loss the quartz concentration profiles for different half-fracture apertures are almost identical and are similar to the temperature profiles in Figure 6(b). Thus, when fluid loss is considered, quartz concentration is not sensitive to the variation in the half-fracture aperture.

Figure 11 to be inserted here

Figure 11 shows the spatial distributions of quartz concentration along the fracture for various rates of inlet discharge. In Figure 11 the equilibrium concentration of quartz is attained nearer to the fracture inlet for high inlet discharges and further away from the fracture for low inlet discharges. This is a result of the different rates at which heat is transferred between the fracture

and the fracture-skin as evident in Figure 7. The results obtained in the absence of fluid loss have not been compared with those obtained with fluid loss because the discharge remains constant when there is no fluid loss and the results obtained would remain constant along the fracture irrespective of the discharge and the temperature profiles would not vary along the fracture.

Influence of fluid loss on pressure and discharge

In this section we summarise the analysis, for the fluid loss case, the influence of inlet discharge on discharge, velocity and pressure along the fracture.

Figure 12 to be inserted here

Figure 12 shows the spatial distributions of discharge in the fracture for various rates of inlet discharges. In all cases the discharge decreases along the fracture because of fluid loss. When the initial discharge rate is high (q = 0.005 $m^3.d^{-1}$), the discharge in the fracture decreases from 0.005 $m^3.d^{-1}$ to 0.003 $m^3.d^{-1}$ at the fracture outlet. For q = 0.0025 $m^3.d^{-1}$, the discharge reduces from 0.0025 $m^3.d^{-1}$. For discharges below 0.001 $m^3.d^{-1}$, the discharge attains zero within a short distance from the fracture inlet. The discharge becomes zero at 5m, 15m, 25m, 35m and 50m from the fracture inlet for respective inlet discharges of 0.0001 $m^3.d^{-1}$, 0.00025 $m^3.d^{-1}$, 0.0005 $m^3.d^{-1}$, 0.00075 $m^3.d^{-1}$, 0.001 $m^3.d^{-1}$. Thus, when fluid loss is considered within the fracture, the initial discharge plays a significant role as it would affect the discharge along the fracture and, in turn, this would affect the fluid velocity, temperature distribution and quartz concentration.

Figure 13 to be inserted here

Figure 13 shows the spatial distributions of fluid velocity in the fracture for various rates of inlet discharges. The velocity is high at the inlet when the inlet discharge is high and subsequently the velocity decreases along the fracture because of fluid loss. The behaviour is similar to that in Figure 12 as velocity along the fracture is based on the inlet discharge in the fracture. Another important point to note here is that the magnitude of the velocity remains low when the discharge is low. When discharge is gradually increased, the velocity rises to a very high magnitude of 50 $m.d^{-1}$, which is very uncommon in a fractured porous media.

Figure 14 to be inserted here

Figure 14 shows the spatial distributions of pressure in the fracture for various rates of inlet discharges. The behaviour of pressure in the fracture is similar to the velocity distribution in Figure 13. The pressure is directly proportional to the fluid discharge according to Eqn. (1) and therefore the pressure in the fracture depends on the discharge pattern within the fracture. The magnitude of the pressure remains low when the discharge is low. When discharge is gradually increased, the pressure reaches a very high magnitude of 70 Pa. Therefore, even a discharge of 0.005 $m^3.d^{-1}$ can lead to high pressure in a geothermal system.

Conclusions

We have analysed the behaviour of quartz concentration in a coupled fracture matrix system in the presence of fracture skin. Coupled equations for thermal transport have been solved using the implicit finite difference method. A varying grid pattern is used to capture the flux transfer at the

interface of the fracture and the fracture-skin. It is assumed that the fractures are saturated. It is assumed that water is pumped at a particular rate with a low temperature at the inlet of the fracture. The effect of fluid loss from the fracture on thermal transport and quartz precipitation has also been analysed in the present study. By considering the combined effects of fracture skin formation and fluid loss, this study has addressed some important practical issues and has produced some very useful results, which extend the work of Natarajan and Suresh Kumar [21,22].

The following conclusions have been drawn from this study.

1. Low fluid velocity provides high residence time for the fluid, which enhances the heat transfer from the fracture-skin to the fracture. On the other hand, high fluid velocity requires a longer time for the fluid to access the heat stored within the fracture-skin and hence the rock matrix.

2. Loss of fluid from the fracture affects the fluid velocity, which in turn affects the heat transfer mechanism and mineral precipitation within the fracture.

3. When fluid loss along the fracture is considered, the rate at which fluid is injected at the inlet of the fracture plays a major role in the heat transfer and chemical reaction within the fracture.

4. The fluid velocity, pressure and discharge follow a similar variation pattern along the fracture for various initial fluid discharges at the inlet of the fracture, though their absolute values are significantly different.

5. When there is fluid loss, the effect of fracture skin formation on the heat transfer mechanism is reduced. Moreover, this effect becomes much less sensitive the variation of the size of fracture apertures, which is an important result from this study.

6. The magnitude of the fracture skin thickness affects the attainment of equilibrium temperature within the fracture in terms of its magnitude and distance from the fracture inlet.

References

[1] Robinson BA (1982) Quartz dissolution and silica deposition in hot dry rock geothermal systems, M.S. thesis, MIT

[2] Robinson BA, Pendergrass J (1989) A combined heat transfer and quartz dissolution/deposition model for a hot dry rock geothermal reservoir. Proceedings of the 14th Stanford Geothermal Workshop, Stanford University, 207–212

[3] Cline JS, Bodnar RJ, Rimstidt D (1992) Numerical simulation of fluid flowand silica transport and deposition in boiling hydrothermal solutions: applications to epithermal gold deposits. J. Geophys. Res 97 (B6): 9085–9103

[4] Malate RCM, O'Sullivan MJ (1992) Mathematical modeling of nonisothermal silica transport and deposition in a porous medium. Geothermics 21: 519–544

[5] Lowell RP, Van Cappellen P, Germanovich LN (1993) Silica precipitation in fractures and the evolution of permeability in hydrothermal upflow zones. Science 260: 192–194.

[6] Arvidson RS, Mackenzie FT (1999) The dolomite problem: the control of precipitation kinetics by temperature and saturation state. American Journal of Science 299: 257-288

[7] Satman A, Ugur Z, Onur M (1999) The Effect of Calcite Deposition on Geothermal Well Inflow Performance. Geothermics 4(1): 425- 444

[8] O'Brien GS, Bean CJ, McDermott F (2003) Numerical investigation of passive and reactive flow through generic single fractures with heterogeneous permeability. Earth and Planetary Science Letters 213: 271-284

[9] Suresh Kumar G, Ghassemi A (2005) Numerical modeling of non-isothermal quartz dissolution in a coupled fracture–matrix system. Geothermics 34:411–439

[10] Ghassemi A, Suresh Kumar G (2007) Changes in fracture aperture and fluid pressure due to thermal stress and silica dissolution/precipitation induced by heat extraction from subsurface rocks. Geothermics 36: 115-140

[11] Taron J, Elsworth D, Min K (2009) Numerical simulation of thermal-hydrologic-mechanical-chemical processes in deformable, fractured porous media. International Journal of Rock Mechanics and Mining sciences 46:842-854

[12] Taron J, Elsworth D (2009) Thermal–hydrologic–mechanical–chemical processes in the evolution of engineered geothermal reservoirs. International Journal of Rock Mechanics and Mining sciences 46: 855-864

[13] Moench AF (1984) Double-Porosity Models for a Fissured Groundwater Reservoir with Fracture Skin. Water Resour. Res. 20:831-846

[14] Moench AF (1983) Well Test Analysis in Naturally Fissured, Geothermal Reservoirs with Fracture Skin. Proc. gth Workshop on Geothermal Reservoir Engineering, Stanford University, Stanford, CA, 175-180

[15] Sharp JM (1993) Fractured aquifers/reservoirs; Approaches,problems, and opportunities. In: Banks,D., Banks,S.(Eds), Hydrogeology of Hard Rocks. Memoires of the 24 th Cong. International Assoc. Hydrogeologists.Oslo Norway 24 part 1: 23-28

[16] Driese SG, McKay LD, Penfield CP (2001) Lithologic and pedogenic influences on porosity distribution and groundwater flow in fractured sedimentary saporolite: a new application of environmental sedimentology. Journal of Sedimentology Research 71(5): 843-857

[17] Fu L, Milliken KL, Sharp Jr JM (1993) Porosity and permeability variations in fractured and liesegang-banded Breathirr sandstones(middle Pennsylvanian), eastern Kentucky : diagenetic controls and implications for modeling dual-porosity systems. Journal of Hydrology 154: 351-381

[18] Robinson NI, Sharp Jr. JM (1997) Analytical solution for contaminant transport in a finite set of parallel fractures with matrix diffusion. C.S.I.R.O. Mathematical and Information Sciences Report CMIS, C23.

[19] Antonellini M, Aydin A (1994) Effect of faulting on fluid flow in porous sandstones: Petrophysical Properties. AmerAssoc. Petrol. Geol. Bull. 78:355-377

[20] Kreisel I, Sharp Jr. JM (1996) Fracture skins in the Brushy Canyon Formation. In: W.D. DeMis and A.G. Cole (Eds.), The Brushy Canyon Play in Outcrop and Subsurface: Concepts and Examples, PBS-SEPM No.96-38, Midland, TX.

[21] Natarajan N, Suresh Kumar G (2011) Numerical modeling and spatial moment analysis of thermal fronts in a coupled fracture-skin-matrix system. Geotechnical and Geological Engineering 29: 477-491

[22] Natarajan N, Suresh Kumar G (2012) Evolution of fracture permeability due to co-colloidal bacterial transport in a coupled fracture-skin-matrix system. Geoscience Frontiers 3: 503-514

[23] Robinson NI, Sharp JM, Kreisel I (1998) Contaminant transport in sets of parallel finite fractures with fracture skins. J. Contam. Hydrol. 31: 83–109

[24] Rawal C, Ghassemi A (2008) Reactive silica transport in hot poroelastic rock and its effects on fracture aperture. GRC Transactions 32: 237-242

[25] Ghassemi A, Tarasovs S, Cheng AD-H (2003) An integral equation method for modeling three-dimensional heat extraction from a fracture in hot dry rock. Int. J. Numer. Anal. Methods Geomech. 27 (12): 989–1004

[26] de Marsily G (1986) Quantitative Hydrogeology: Groundwater Hydrology for Engineers Academic Press Inc., San Diego, CA, USA

[27] Rimstidt JD, Barnes HL (1980) The kinetics of silica-water reactions. Geochim. Cosmochim. Acta, 44:1683–1699

Table captions

Table 1 Input parameters used for numerical model

Figure captions

Fig. 1 Schematic diagram showing a coupled fracture-skin-matrix system

Fig. 2 Validation of relative quartz concentration obtained from the numerical model with results

of Kumar and Ghassemi [9] for a coupled fracture matrix system for different simulation times. Parameter values used in the simulation are given in Table 1.

Fig. 3 Comparison of spatial distributions of quartz concentration obtained along the fracture in the presence and absence of fracture skin. Parameter values used in the simulations are given in Table 1.

Fig. 4 Spatial distributions of relative temperature along the fracture for various fluid skin thermal conductivities (a) without fluid loss and (b) with fluid loss. Parameter values used in the simulations are given in Table 1.

Fig. 5 Spatial distributions of relative temperature along the fracture for various initial fluid velocities without fluid loss. Parameter values used in the simulations are given in Table 1.

Fig. 6 Spatial distributions of relative temperature along the fracture for various half fracture apertures (a) without fluid loss and (b) with fluid loss. Parameter values used in the simulations are given in Table 1.

Fig. 7 Spatial distributions of relative temperature along the fracture for various inlet discharge rates. Parameter values used in the simulations are given in Table 1.

Fig. 8 Spatial distributions of quartz concentration along the fracture for various fluid skin thermal conductivities (a) without fluid loss and (b) with fluid loss. Parameter values used in the simulations are given in Table 1.

Fig. 9 Spatial distributions of quartz concentration along the fracture for various initial fluid velocities. Parameter values used in the simulations are given in Table 1.

Fig. 10 Spatial distributions of quartz concentration along the fracture for various half-fracture apertures (a) without fluid loss and (b) with fluid loss. Parameter values used in the simulations are given in Table 1.

Fig. 11 Spatial distributions of quartz concentration along the fracture for various inlet discharge rates. Parameter values used in the simulations are given in Table 1.

Fig. 12 Spatial distributions of discharge in the fracture for various inlet discharge rates. Parameter values used in the simulations are given in Table 1.

Fig. 13 Spatial distributions of fluid velocity in the fracture for various inlet discharge rates. Parameter values used in the simulations are given in Table 1.

Fig. 14 Spatial distributions of pressure in the fracture for various inlet discharge rates. Parameter values used in the simulations are given in Table 1.

Table 1 Input parameters used for numerical model

Parameter	Symbol	Value	Units
Initial half fracture aperture	b	100	μm
Thermal dispersivity	β_T	0.05	m
Rock matrix specific heat capacity	C_m	800	$J.kg^{-1}.K^{-1}$
Rock density	ρ_m	2600	$kg.m^{-3}$
Thermal conductivity of the rock matrix	λ_m	2	$W.(m\text{-}K)^{-1}$
Specific heat capacity of the fracture-skin	C_s	1500	$J.kg^{-1}.K^{-1}$
Fracture-skin density	ρ_s	1500	$kg.m^{-3}$
Thermal conductivity of the fracture-skin	λ_s	10	$W.(m\text{-}K)^{-1}$
Rock matrix porosity	θ	0.05	-
Porosity of fracture-skin	θ_s	0.1	-
Specific heat capacity of fracture fluid	C_f	5000	$J^{-1}.kg^{-1}.K^{-1}$
Fracture fluid density	ρ_f	1000	$kg.m^{-3}$
Thermal conductivity of fracture fluid	λ_f	0.5	$W.(m\text{-}K)^{-1}$
Initial temperature (matrix and fracture)	T_0	600	K
Temperature at the inlet of the fracture	T_i	300	K
Length of the fracture	L	50	m
Total simulation time	T	25	days

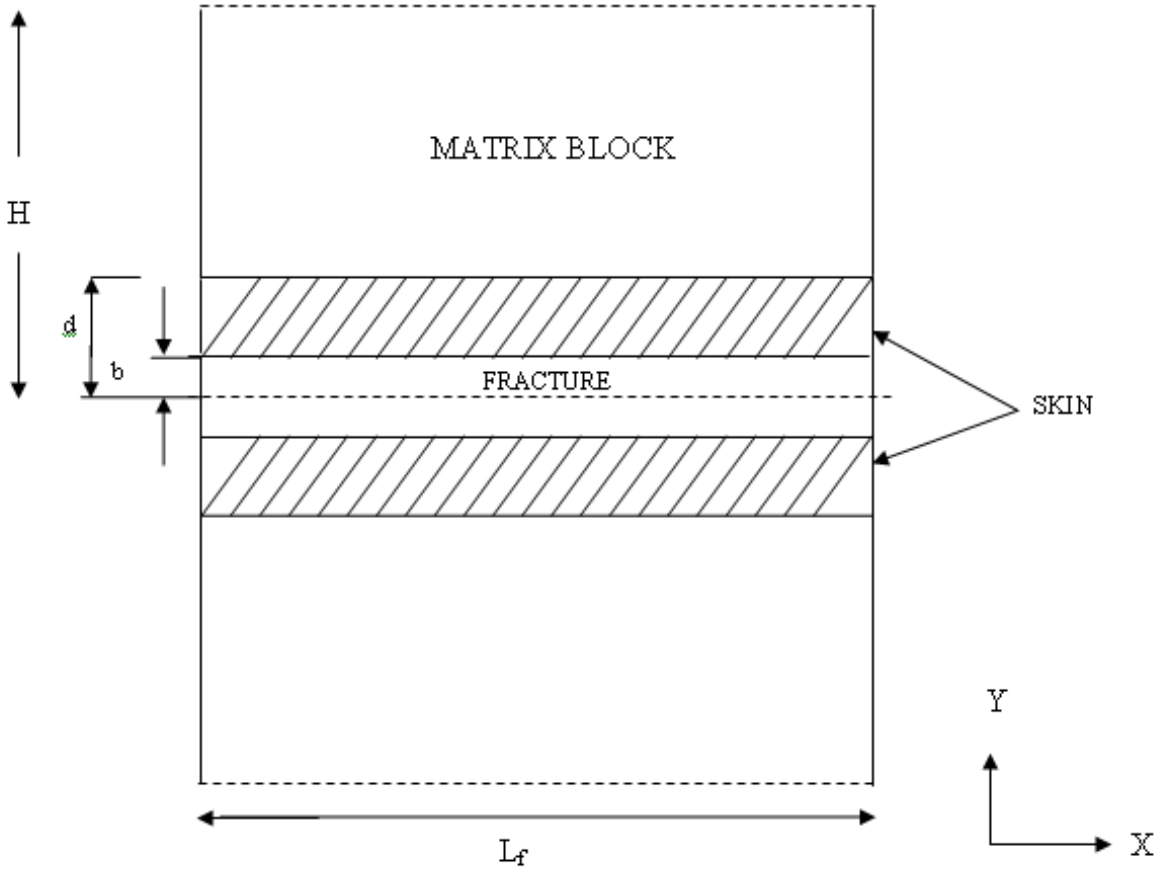

Figure 1

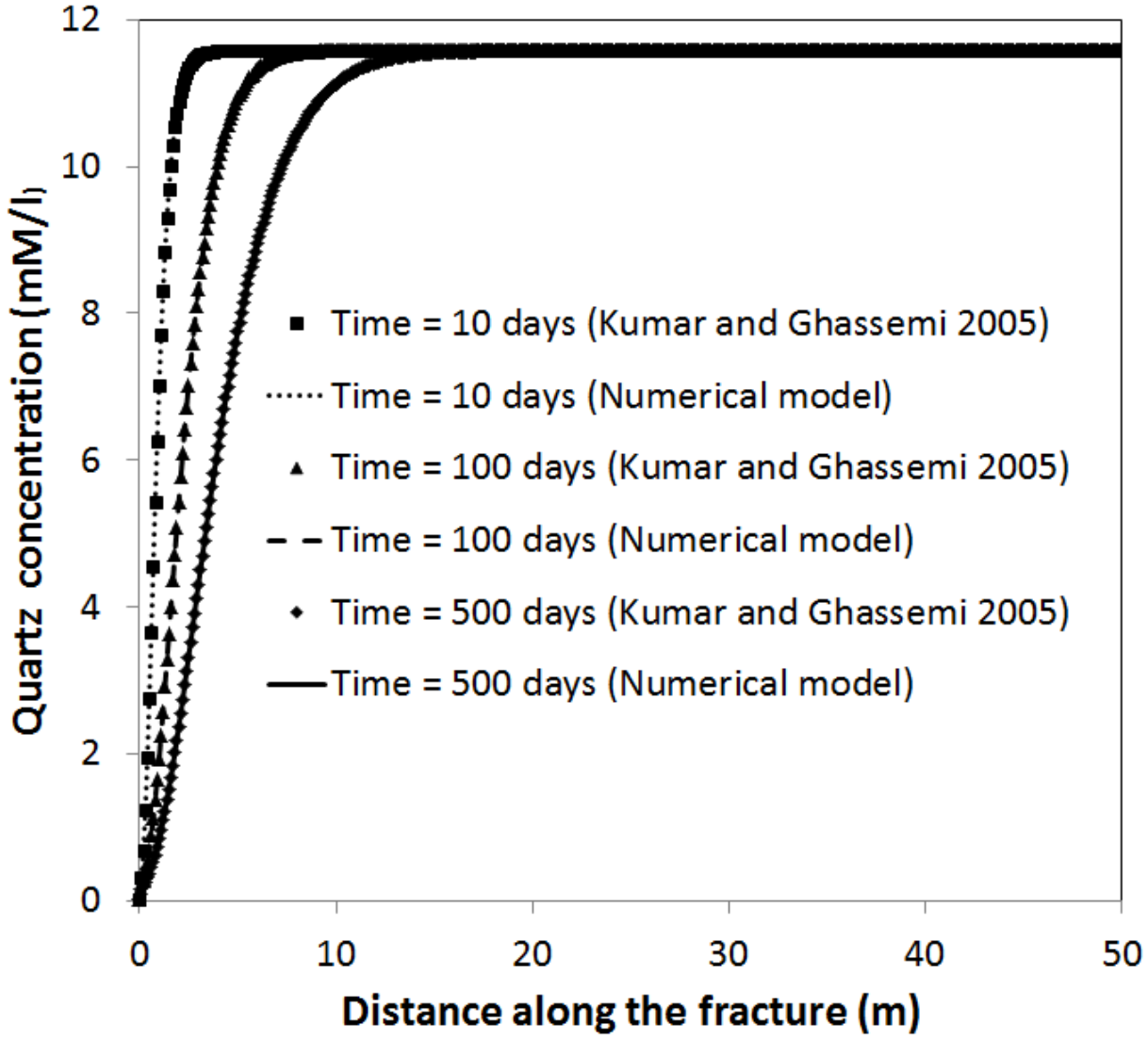
12
10
8
6
4
2
0
Quartz concentration (mM/l)
0
10
20
30
40
50
Distance along the fracture (m)
Time = 10 days (Kumar and Ghassemi 2005)
Time = 10 days (Numerical model)
Time = 100 days (Kumar and Ghassemi 2005)
Time = 100 days (Numerical model)
Time = 500 days (Kumar and Ghassemi 2005)
Time = 500 days (Numerical model)

Figure 2

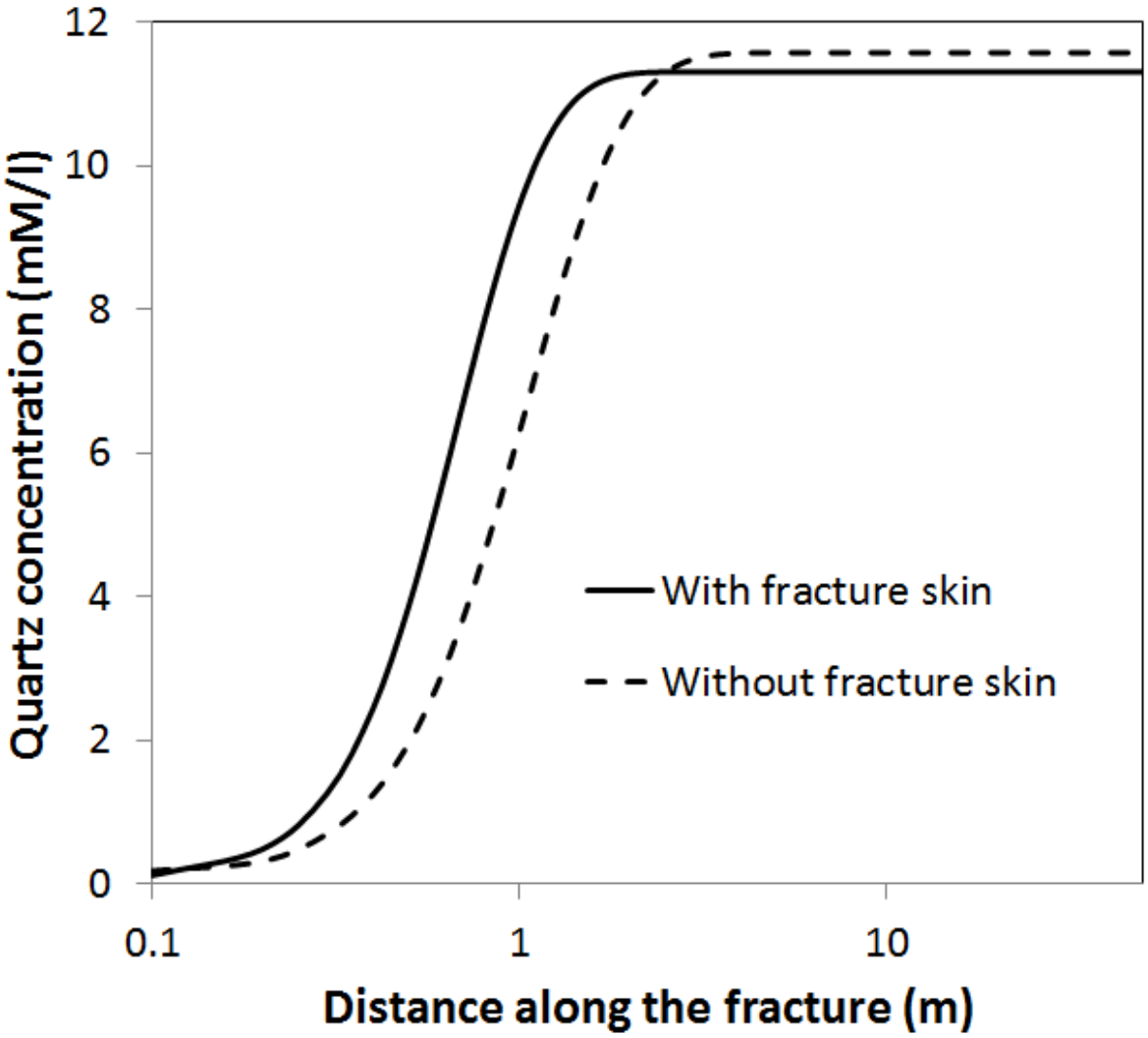
12
10
8
6
4
2
0
Quartz concentration (mM/l)
0.1
1
10
Distance along the fracture (m)
With fracture skin
Without fracture skin

Figure 3

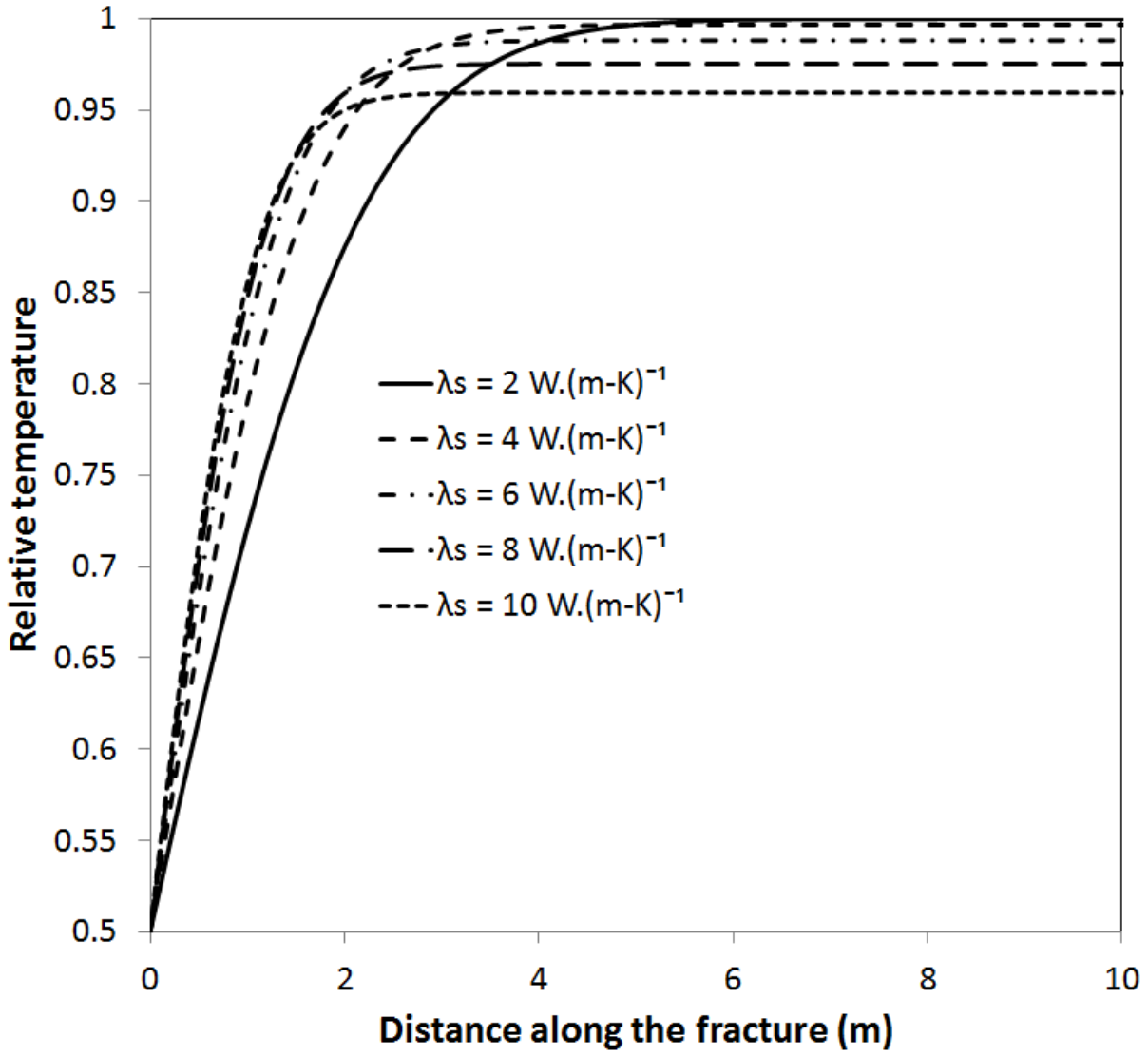
Relative temperature
Distance along the fracture (m)
λs = 2 W.(m-K)⁻¹
λs = 4 W.(m-K)⁻¹
λs = 6 W.(m-K)⁻¹
λs = 8 W.(m-K)⁻¹
λs = 10 W.(m-K)⁻¹
1
0.95
0.9
0.85
0.8
0.75
0.7
0.65
0.6
0.55
0.5
0
2
4
6
8
10

Figure 4a

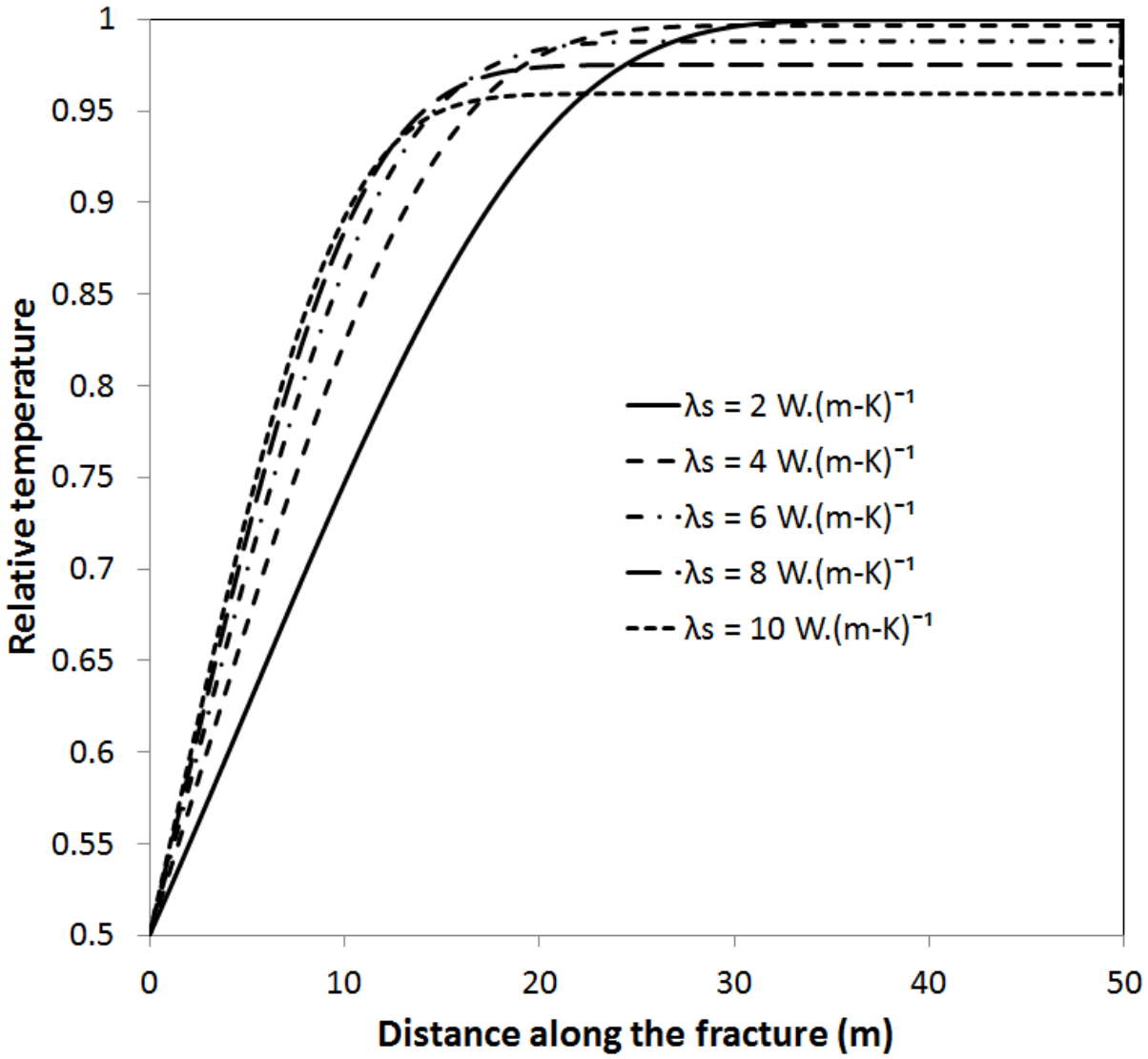
Relative temperature
1
0.95
0.9
0.85
0.8
0.75
0.7
0.65
0.6
0.55
0.5
0
10
20
30
40
50
Distance along the fracture (m)
λs = 2 W.(m-K)⁻¹
λs = 4 W.(m-K)⁻¹
λs = 6 W.(m-K)⁻¹
λs = 8 W.(m-K)⁻¹
λs = 10 W.(m-K)⁻¹

Figure 4b

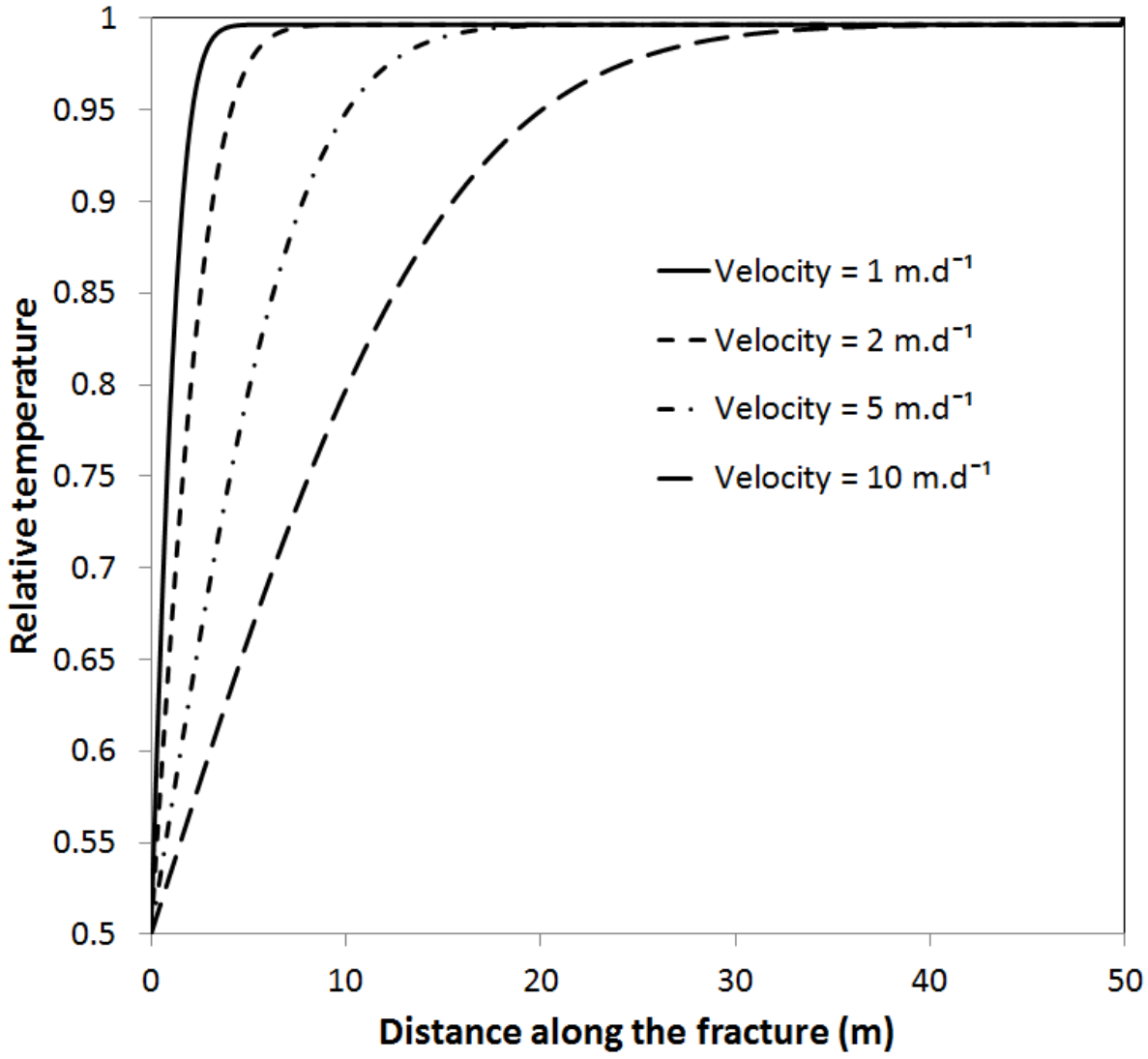
Relative temperature
1
0.95
0.9
0.85
0.8
0.75
0.7
0.65
0.6
0.55
0.5
0
10
20
30
40
50
Distance along the fracture (m)
Velocity = 1 m.d-1
Velocity = 2 m.d-1
Velocity = 5 m.d-1
Velocity = 10 m.d-1

Figure 5

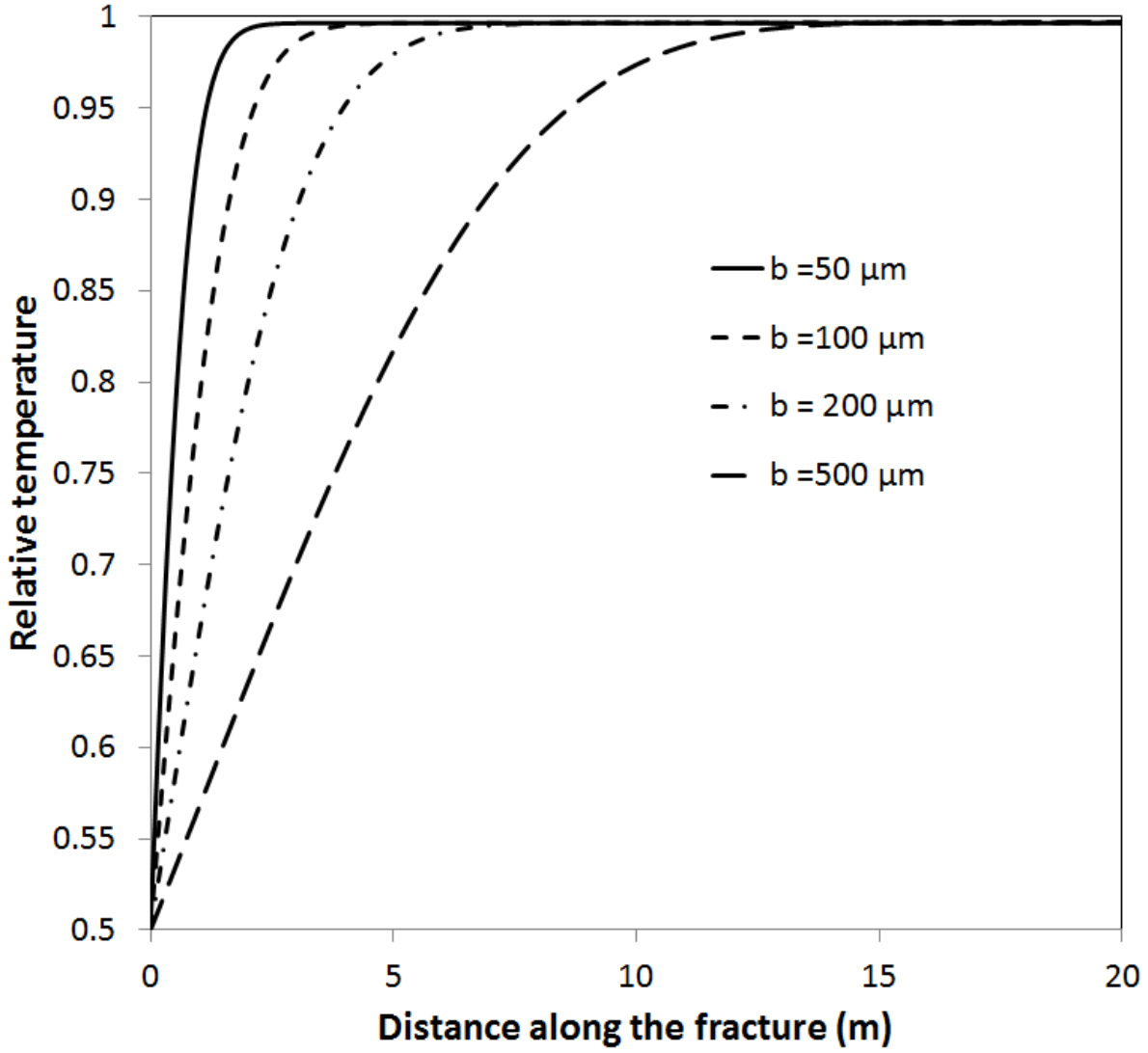
1
0.95
0.9
0.85
0.8
0.75
0.7
0.65
0.6
0.55
0.5
Relative temperature
0
5
10
15
20
Distance along the fracture (m)
b =50 µm
b =100 µm
b = 200 µm
b =500 µm

Figure 6a

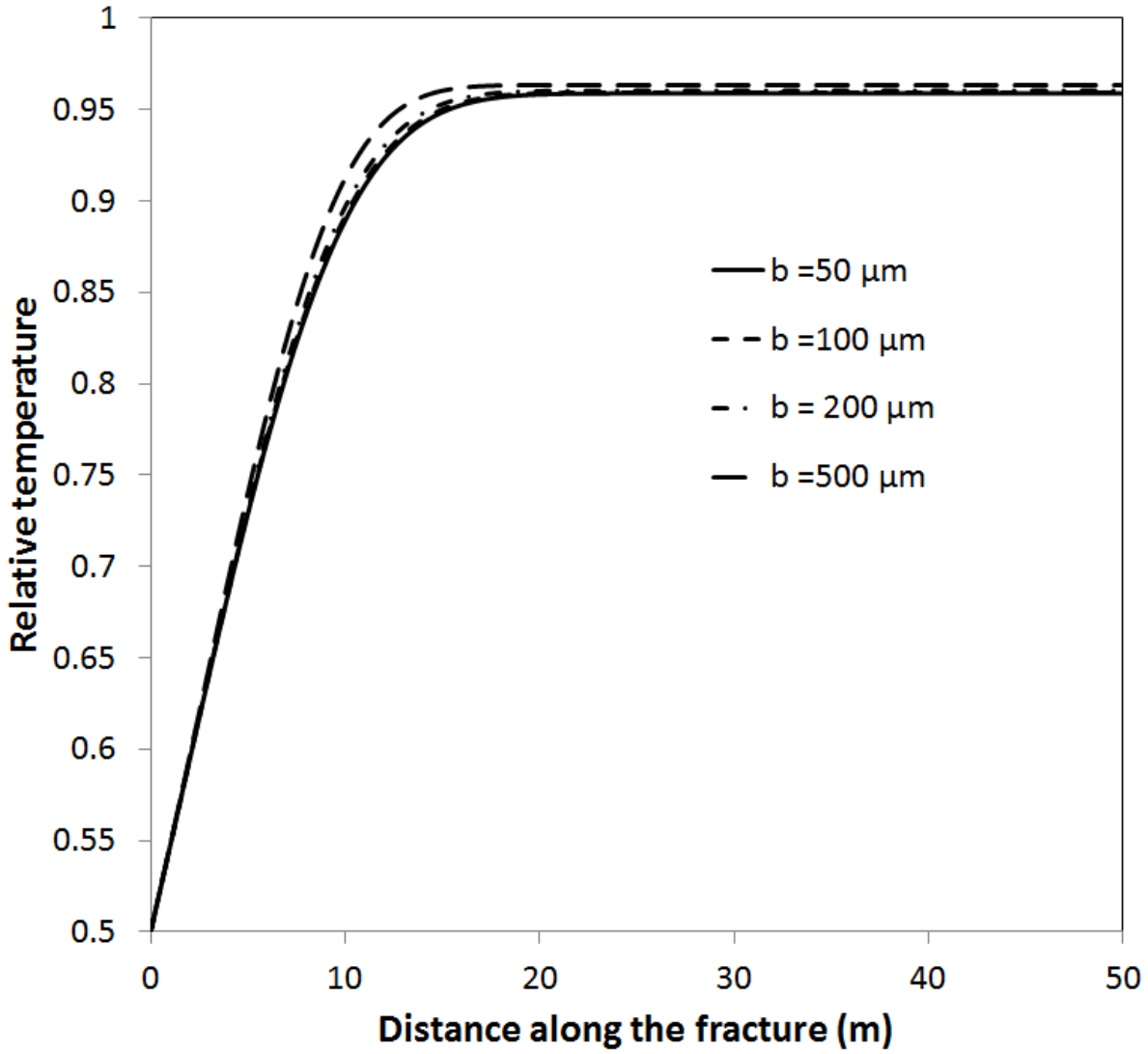
1
0.95
0.9
0.85
0.8
0.75
0.7
0.65
0.6
0.55
0.5
Relative temperature
0
10
20
30
40
50
Distance along the fracture (m)
b =50 µm
b =100 µm
b = 200 µm
b =500 µm

Figure 6b

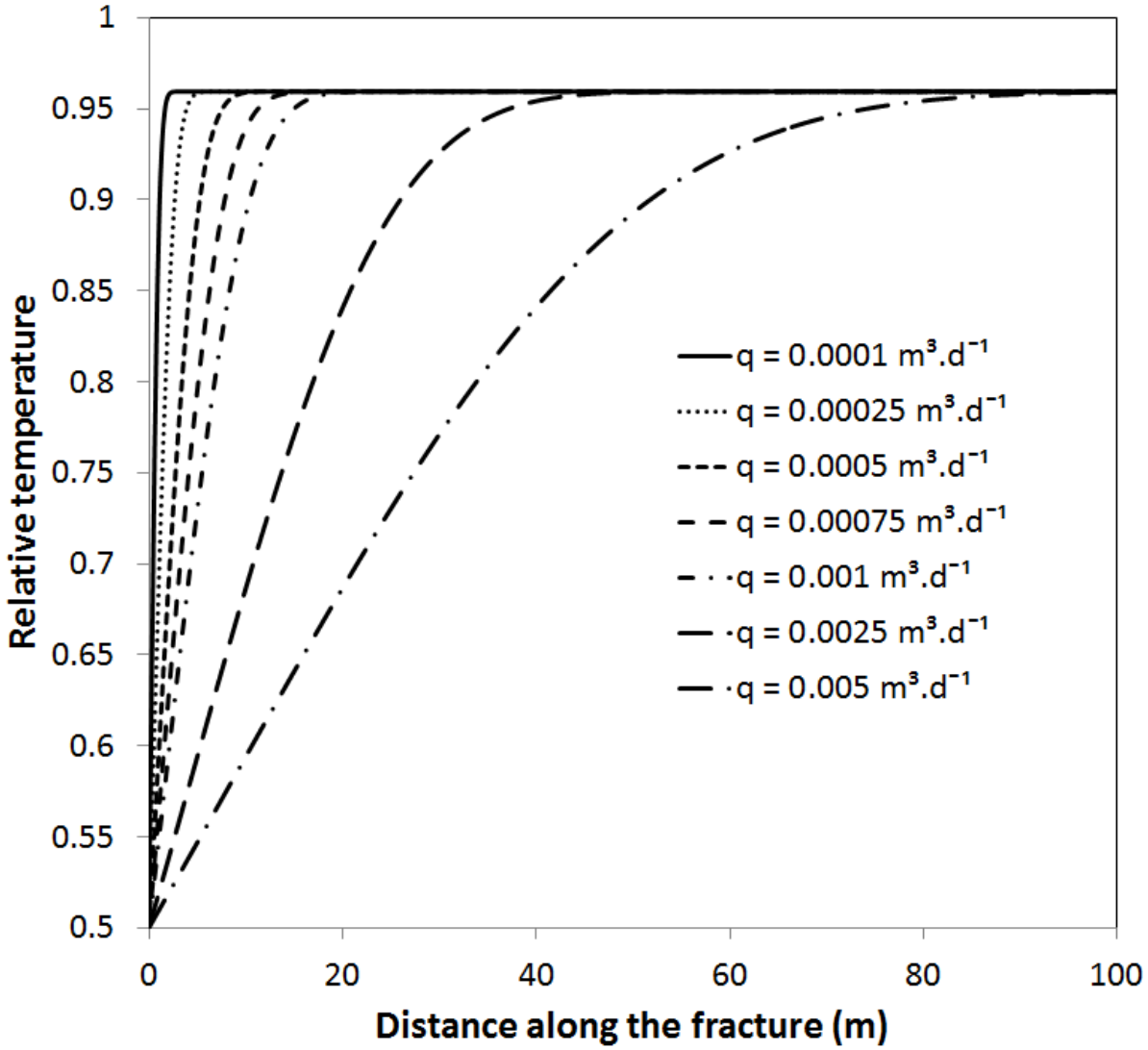
1
0.95
0.9
0.85
0.8
0.75
0.7
0.65
0.6
0.55
0.5
Relative temperature
0
20
40
60
80
100
Distance along the fracture (m)
q = 0.0001 m³.d⁻¹
q = 0.00025 m³.d⁻¹
q = 0.0005 m³.d⁻¹
q = 0.00075 m³.d⁻¹
q = 0.001 m³.d⁻¹
q = 0.0025 m³.d⁻¹
q = 0.005 m³.d⁻¹

Figure 7

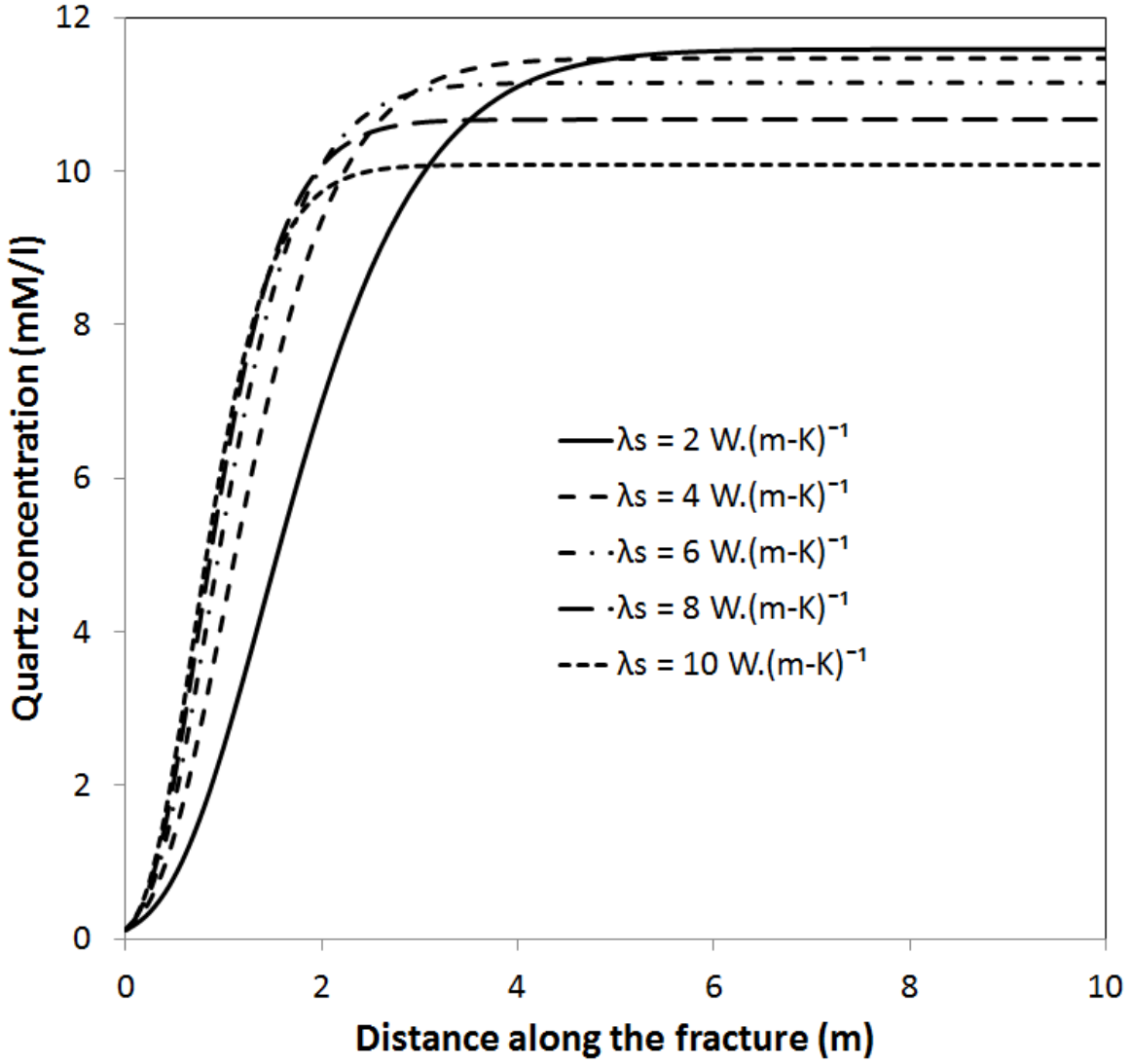
12
10
8
6
4
2
0
0
2
4
6
8
10
Quartz concentration (mM/l)
Distance along the fracture (m)
λs = 2 W.(m-K)⁻¹
λs = 4 W.(m-K)⁻¹
λs = 6 W.(m-K)⁻¹
λs = 8 W.(m-K)⁻¹
λs = 10 W.(m-K)⁻¹

Figure 8a

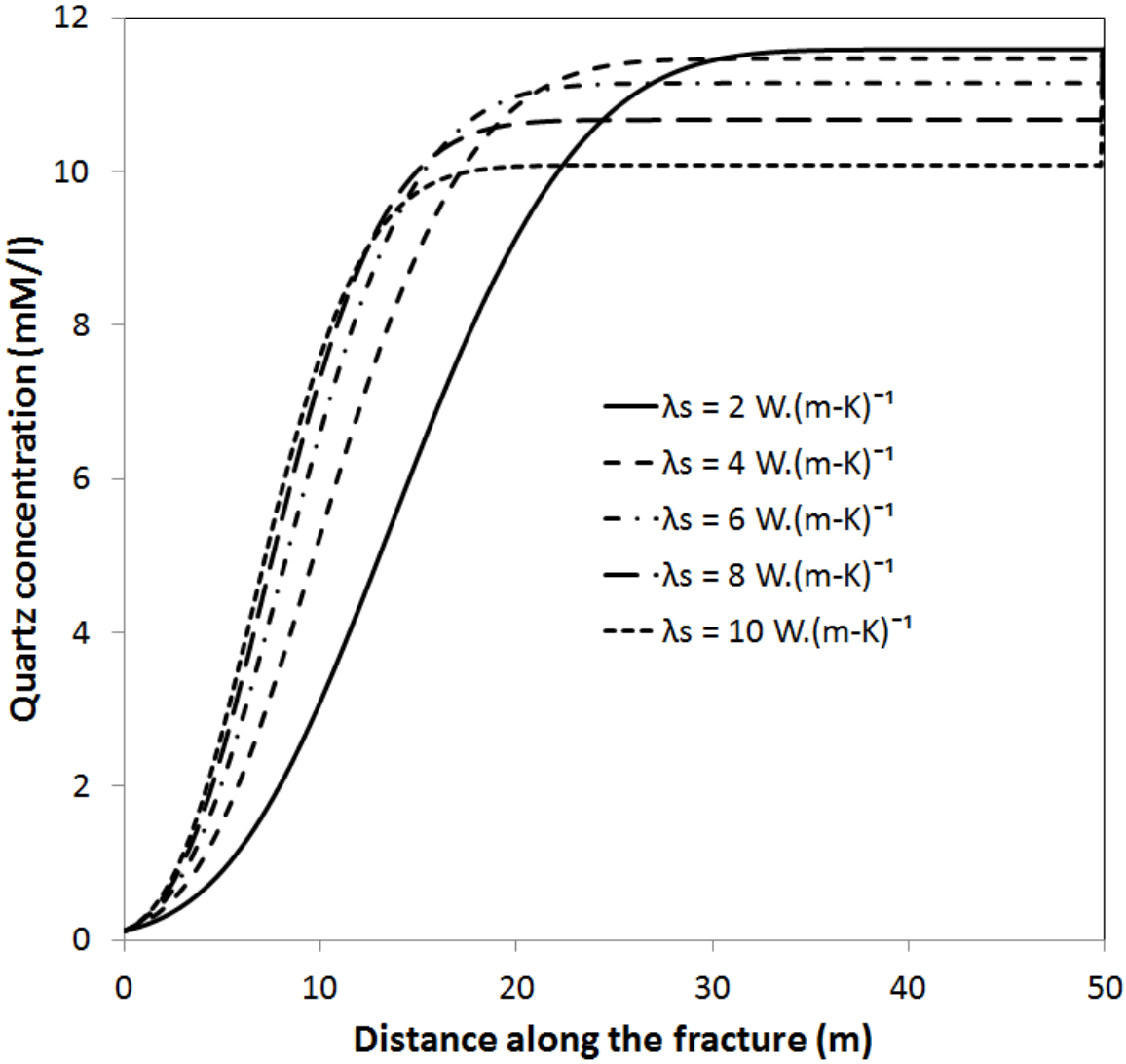
12
10
8
6
4
2
0
0
10
20
30
40
50
Quartz concentration (mM/l)
Distance along the fracture (m)
λs = 2 W.(m-K)⁻¹
λs = 4 W.(m-K)⁻¹
λs = 6 W.(m-K)⁻¹
λs = 8 W.(m-K)⁻¹
λs = 10 W.(m-K)⁻¹

Figure 8b

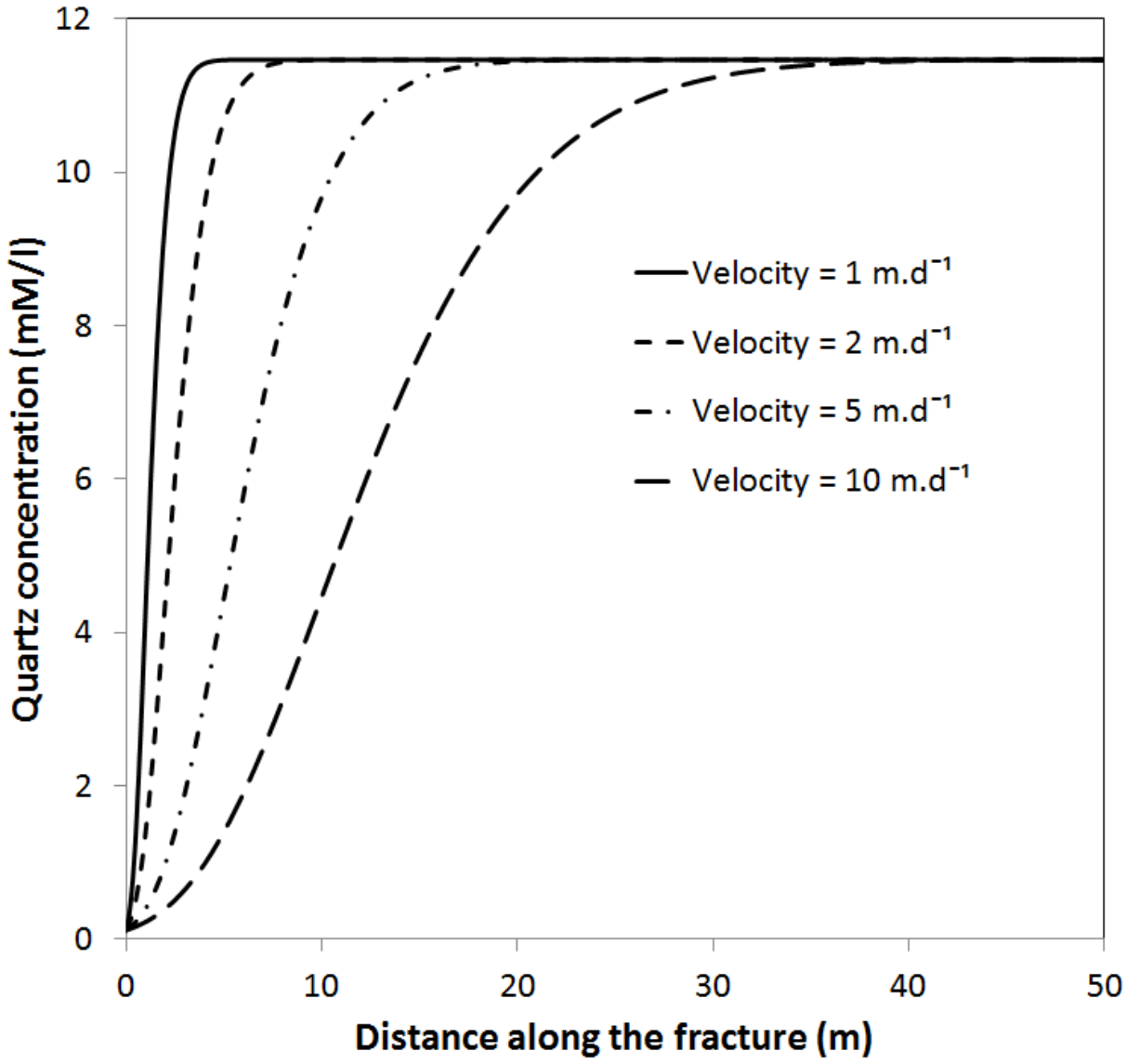
Quartz concentration (mM/l)
Distance along the fracture (m)
Velocity = 1 m.d-1
Velocity = 2 m.d-1
Velocity = 5 m.d-1
Velocity = 10 m.d-1
0
2
4
6
8
10
12
0
10
20
30
40
50

Figure 9

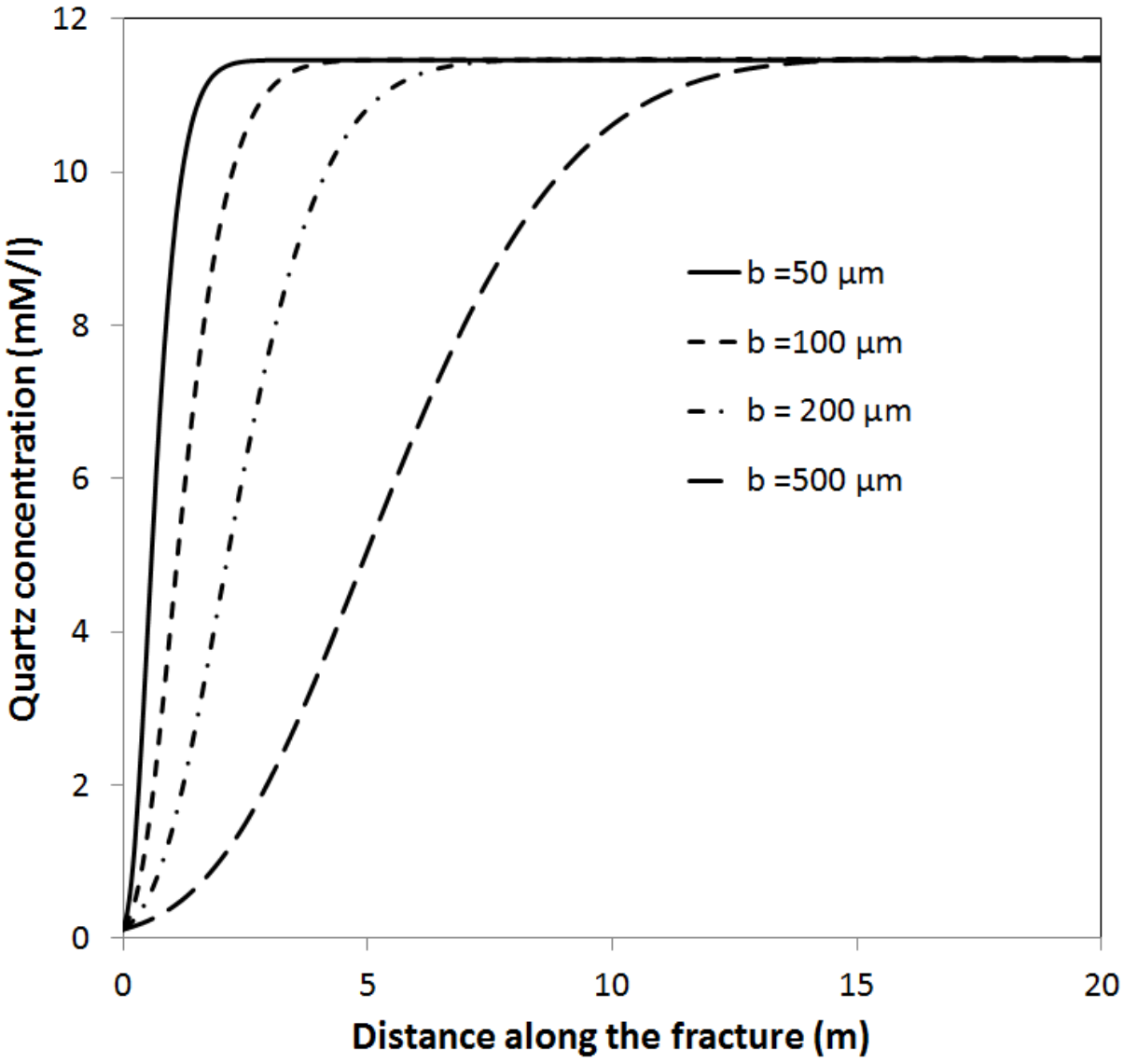
12
10
8
6
4
2
0
Quartz concentration (mM/l)
0
5
10
15
20
Distance along the fracture (m)
b =50 µm
b =100 µm
b = 200 µm
b =500 µm

Figure 10a

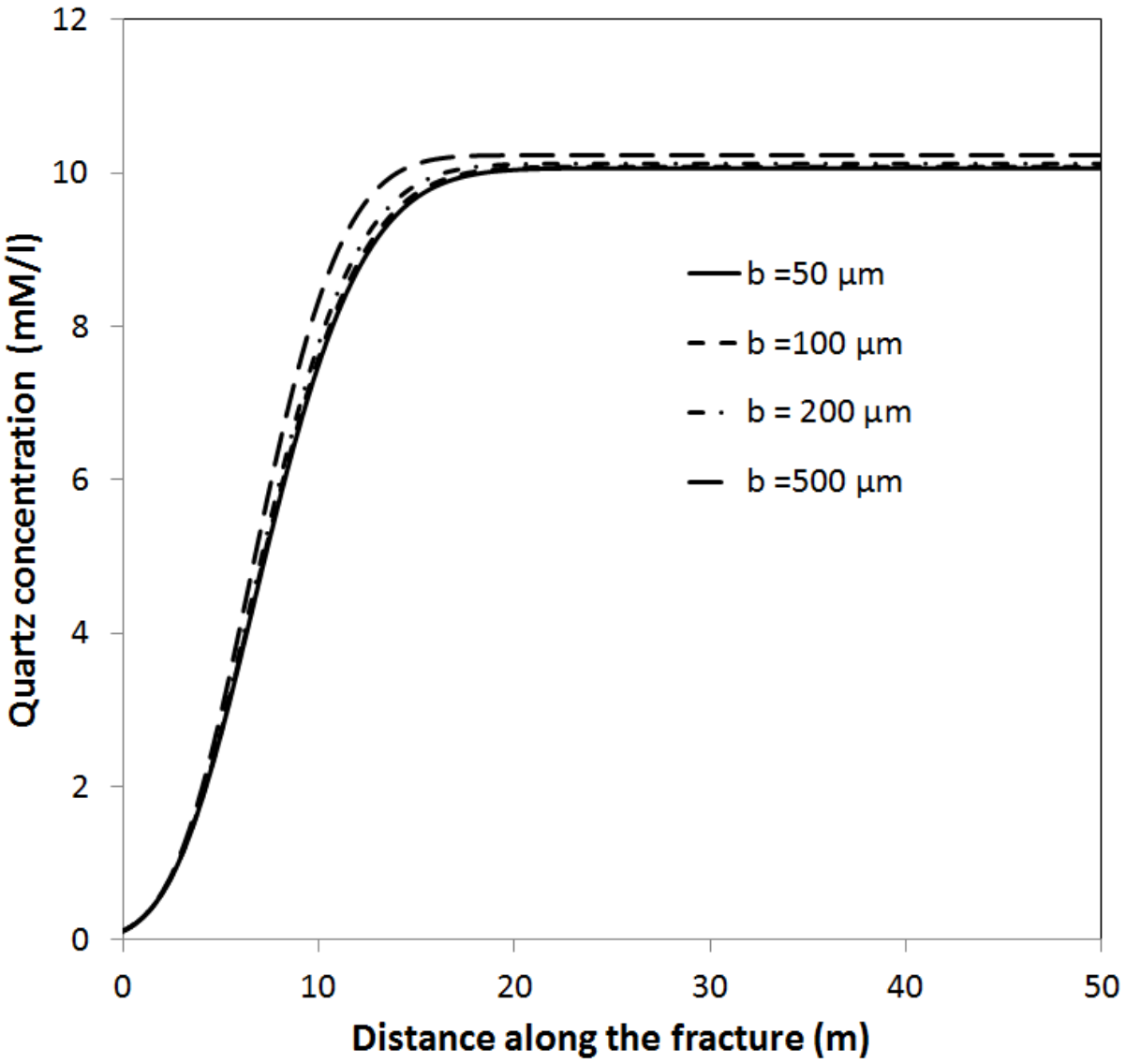
12
10
8
6
4
2
0
0
10
20
30
40
50
Quartz concentration (mM/l)
Distance along the fracture (m)
b =50 µm
b =100 µm
b = 200 µm
b =500 µm

Figure 10b

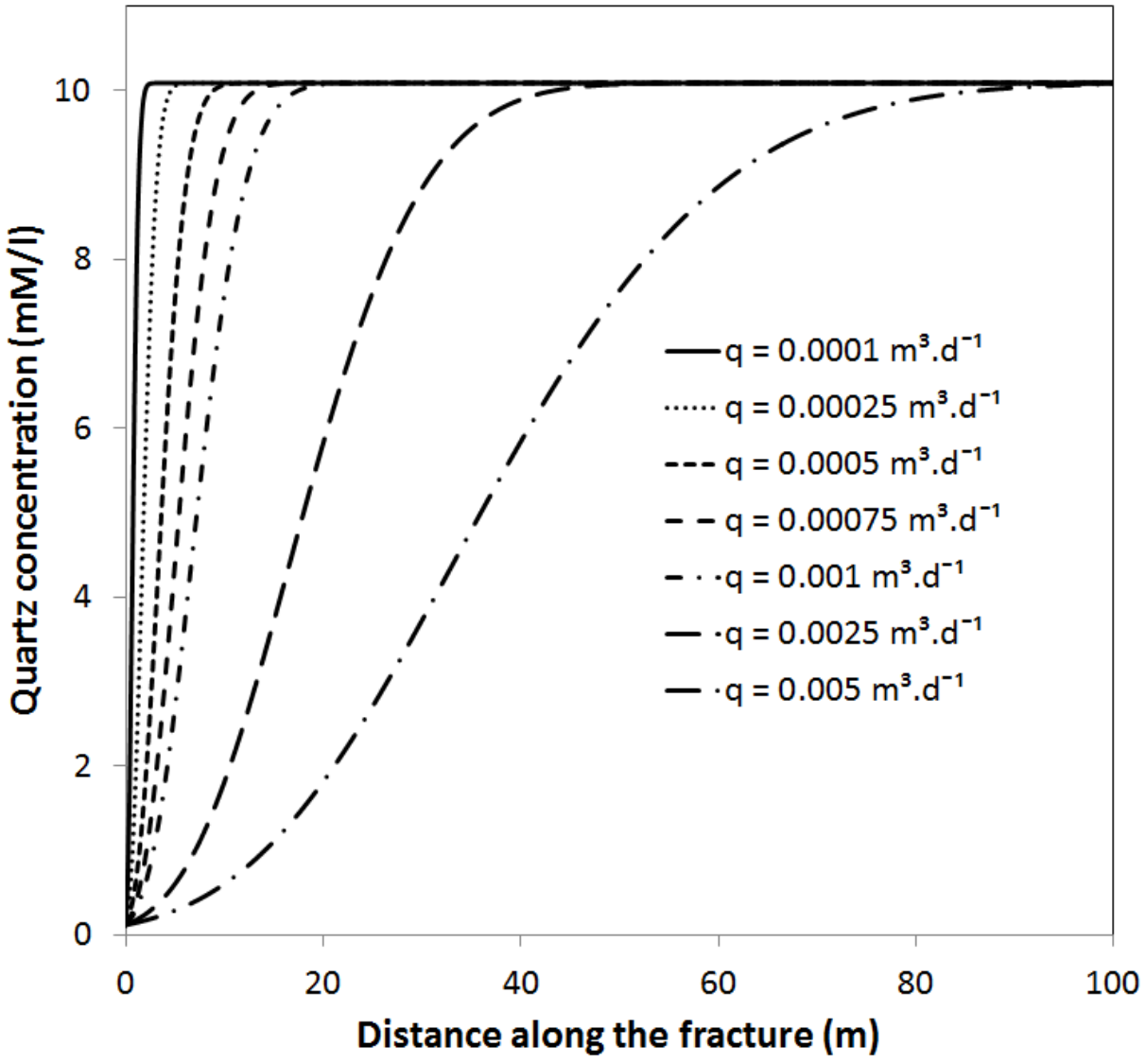
Quartz concentration (mM/l)
Distance along the fracture (m)
0
2
4
6
8
10
0
20
40
60
80
100
q = 0.0001 m³.d⁻¹
q = 0.00025 m³.d⁻¹
q = 0.0005 m³.d⁻¹
q = 0.00075 m³.d⁻¹
q = 0.001 m³.d⁻¹
q = 0.0025 m³.d⁻¹
q = 0.005 m³.d⁻¹

Figure 11

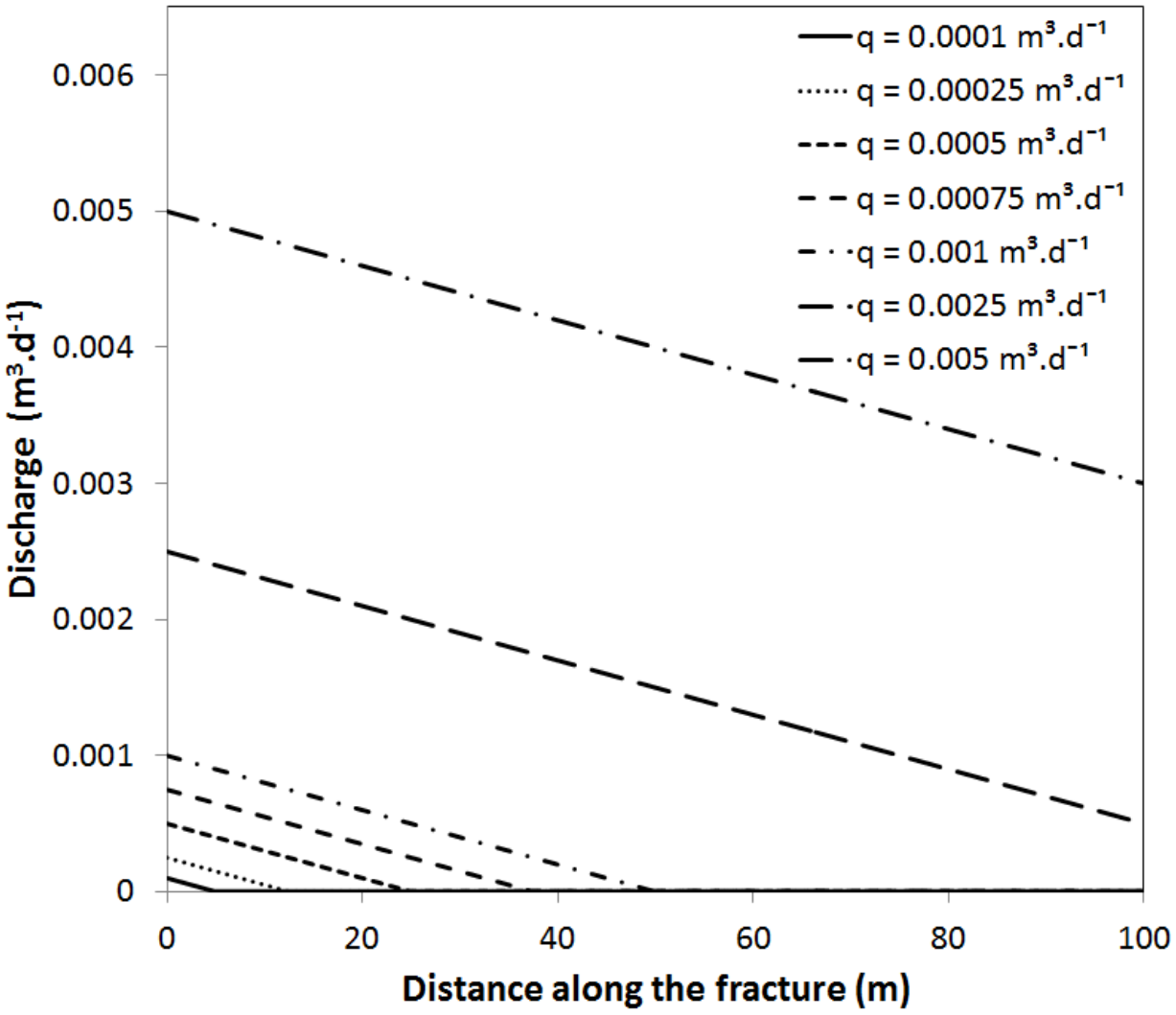
q = 0.0001 m³.d⁻¹
q = 0.00025 m³.d⁻¹
q = 0.0005 m³.d⁻¹
q = 0.00075 m³.d⁻¹
q = 0.001 m³.d⁻¹
q = 0.0025 m³.d⁻¹
q = 0.005 m³.d⁻¹
Discharge (m³.d⁻¹)
0.006
0.005
0.004
0.003
0.002
0.001
0
0
20
40
60
80
100
Distance along the fracture (m)

Figure 12

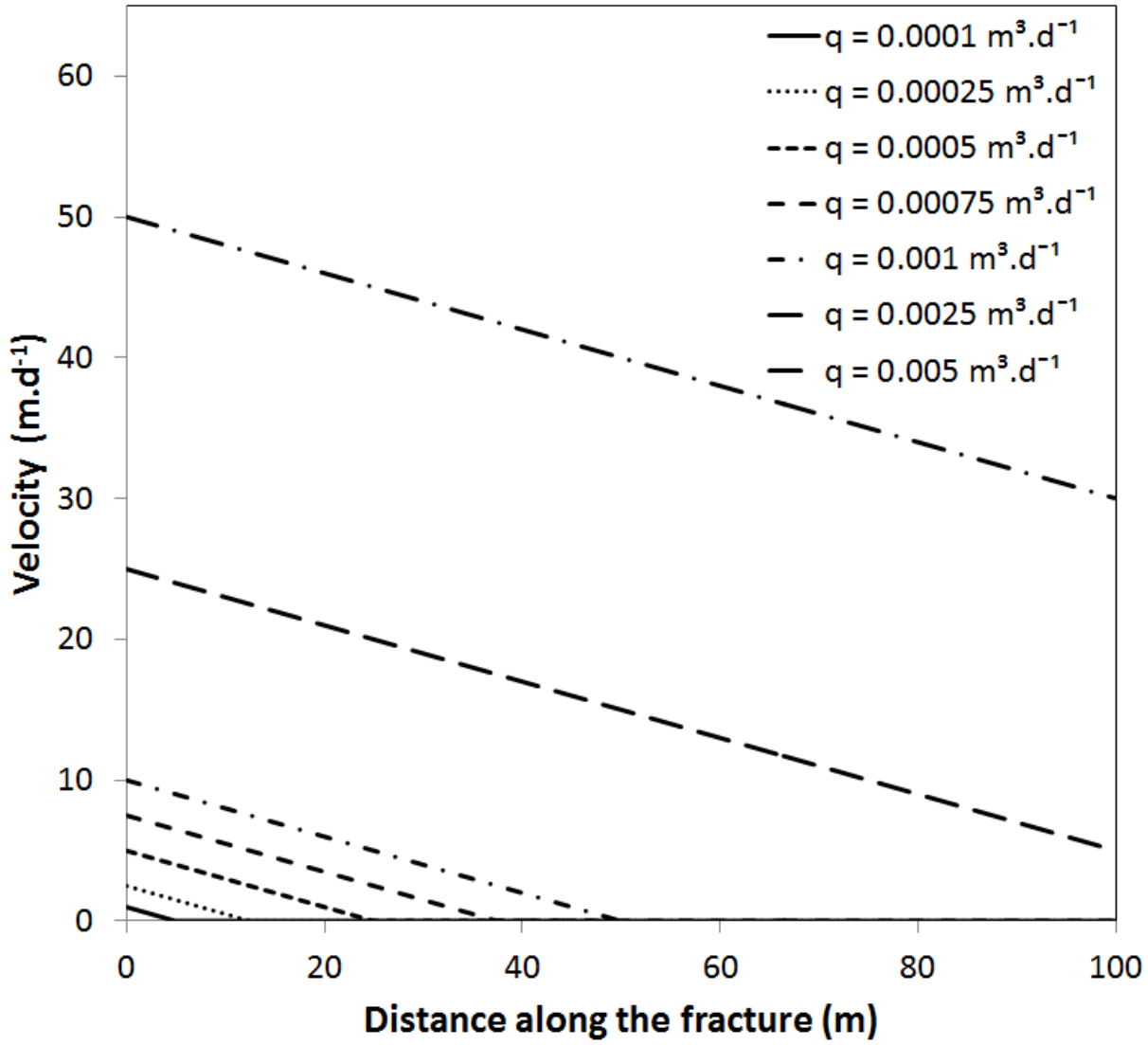
q = 0.0001 m³.d⁻¹
q = 0.00025 m³.d⁻¹
q = 0.0005 m³.d⁻¹
q = 0.00075 m³.d⁻¹
q = 0.001 m³.d⁻¹
q = 0.0025 m³.d⁻¹
q = 0.005 m³.d⁻¹
Velocity (m.d⁻¹)
0
10
20
30
40
50
60
0
20
40
60
80
100
Distance along the fracture (m)

Figure 13

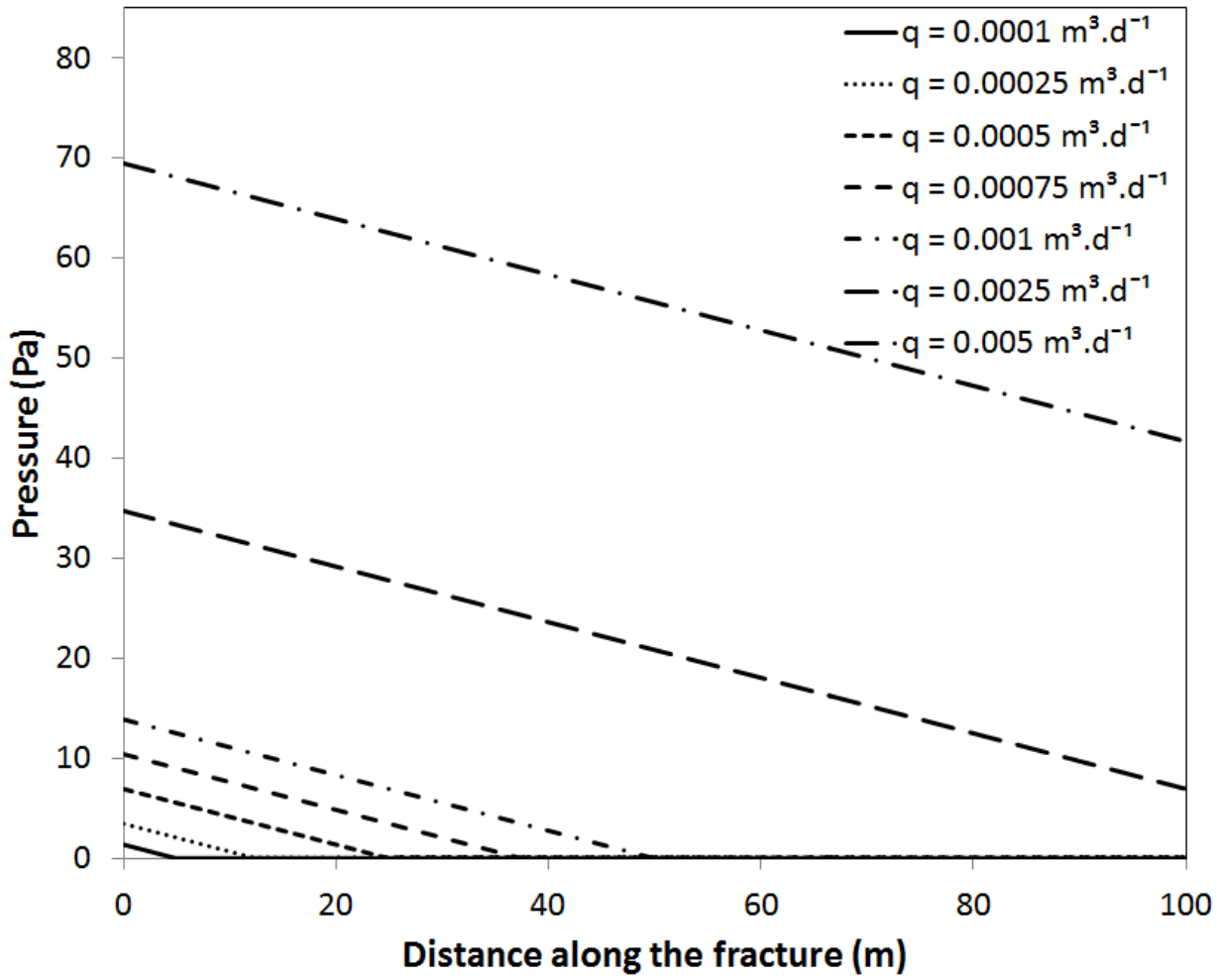
q = 0.0001 m³.d⁻¹
q = 0.00025 m³.d⁻¹
q = 0.0005 m³.d⁻¹
q = 0.00075 m³.d⁻¹
q = 0.001 m³.d⁻¹
q = 0.0025 m³.d⁻¹
q = 0.005 m³.d⁻¹
Pressure (Pa)
0
10
20
30
40
50
60
70
80
0
20
40
60
80
100
Distance along the fracture (m)

Figure 14